A&A 659, A46 (2022)
https://doi.org/10.1051/0004-6361/202142482

Astronomy & Astrophysics

A Virgo Environmental Survey Tracing Ionised Gas Emission (VESTIGE)

XII. Ionised gas emission in the inner regions of lenticular galaxies⋆,⋆⋆

A. Boselli[1], M. Fossati[2], A. Longobardi[1,2], K. Kianfar[3,4], N. Z. Dametto[5], P. Amram[1], J. P. Anderson[6], P. Andreani[4], S. Boissier[1], M. Boquien[5], V. Buat[1], G. Consolandi[2], L. Cortese[7,8], P. Côté[9], J. C. Cuillandre[10], L. Ferrarese[9], L. Galbany[11,12], G. Gavazzi[2], S. Gwyn[9], G. Hensler[13], J. Hutchings[9], E. W. Peng[14], J. Postma[15], J. Roediger[9], Y. Roehlly[1], P. Serra[16], and G. Trinchieri[17]

[1] Aix Marseille Univ, CNRS, CNES, LAM, Marseille, France
e-mail: alessandro.boselli@lam.fr
[2] Universitá di Milano-Bicocca, piazza della scienza 3, 20100 Milano, Italy
[3] Instituto Tecnológico de Aeronáutica (ITA), São José dos Campos, Sao Paolo, Brazil
[4] European Southern Observatory, Karl-Schwarzschild-Strasse 2, 85748 Garching, Germany
[5] Centro de Astronomiá (CITEVA), Universidad de Antofagasta, Avenida Angamos 601, Antofagasta, Chile
[6] European Southern Observatory, Alonso de Córdova 3107, Casilla 19, Santiago, Chile
[7] International Centre for Radio Astronomy Research, The University of Western Australia, 35 Stirling Hw, 6009 Crawley, Australia
[8] ARC Centre of Excellence for All Sky Astrophysics in 3 Dimensions (ASTRO 3D), Australia
[9] National Research Council of Canada, Herzberg Astronomy and Astrophysics, 5071 West Saanich Road, Victoria, BC V9E 2E7, Canada
[10] AIM, CEA, CNRS, Université Paris-Saclay, Université Paris Diderot, Sorbonne Paris Cité, Observatoire de Paris, PSL University, 91191 Gif-sur-Yvette Cedex, France
[11] Institute of Space Sciences (ICE, CSIC), Campus UAB, Carrer de Can Magrans, s/n, 08193 Barcelona, Spain
[12] Institut d'Estudis Espacials de Catalunya (IEEC), 08034 Barcelona, Spain
[13] Department of Astrophysics, University of Vienna, Türkenschanzstrasse 17, 1180 Vienna, Austria
[14] Department of Astronomy, Peking University, Beijing 100871, PR China
[15] University of Calgary, 2500 University Drive NW, Calgary, Alberta, Canada
[16] Osservatorio Astronomico di Cagliari, Via della scienza 5, 09047 Selargius, Cagliari, Italy
[17] INAF – Osservatorio Astronomico di Brera, Via Brera 28, 20159 Milano, Italy

Received 19 October 2021 / Accepted 9 November 2021

ABSTRACT

As part of the Virgo Cluster Survey Tracing Ionised Gas Emission, a blind narrow-band Hα+[NII] imaging survey of the Virgo cluster carried out with MegaCam at the CFHT, we discovered eight massive ($10^{10} \lesssim M_{\rm star} \lesssim 10^{11}\,M_\odot$) lenticular galaxies with prominent ionised gas emission features in their inner (a few kiloparsec) regions. These features are either ionised gas filaments similar to those observed in cooling flows (two galaxies), or they are thin discs with sizes $0.7 \lesssim R({\rm H}\alpha) \lesssim 2.0$ kpc (six galaxies), thus significantly smaller than those of the stellar disc ($R({\rm H}\alpha) \simeq 7 - 22\%R_{\rm iso}(r)$). The morphological properties of these discs are similar to those of the dust seen in absorption in high-resolution HST images. Using a unique set of multifrequency data, including new or archival ASTROSAT/UVIT, GALEX, HST, CFHT, *Spitzer*, and *Herschel* imaging data, combined with IFU (MUSE, ALMA) and long-slit (SOAR) spectroscopy, we show that while the gas that is located within these inner discs is photoionised by young stars, which signals ongoing star formation, the gas in the filamentary structures is shock ionised. The star formation surface brightness of these discs is similar to that observed in late-type galaxies. Because of their reduced size, however, these lenticular galaxies are located below the main sequence of unperturbed or cluster star-forming systems. By comparing the dust masses measured from absorption maps in optical images, from the Balmer decrement, or estimated by fitting the UV-to-far-IR spectral energy distribution of the target galaxies, we confirm that the dust masses derived from optical attenuation maps are heavily underestimated because of geometrical effects due to the relative distribution of the absorbing dust and the emitting stars. We also show that these galaxies have gas-to-dust ratios of $G/D \simeq 80^{320}_{30}$, and that the star formation within these discs follows the Schmidt relation, but with an efficiency that is reduced by a factor of ~2.5. Using our unique set of multifrequency data, we discuss the possible origin of the ionised gas in these objects, which suggests multiple and complex formation scenarios for massive lenticular galaxies in clusters.

Key words. galaxies: elliptical and lenticular, cD – galaxies: ISM – galaxies: evolution – galaxies: interactions – galaxies: clusters: general – galaxies: clusters: individual: Virgo

⋆ The reduced images are only available at the CDS via anonymous ftp to cdsarc.u-strasbg.fr (130.79.128.5) or via http://cdsarc.u-strasbg.fr/viz-bin/cat/J/A+A/659/A46

⋆⋆ Based on observations obtained with MegaPrime/MegaCam, a joint project of CFHT and CEA/DAPNIA, at the Canada-French-Hawaii Telescope (CFHT) which is operated by the National Research Council (NRC) of Canada, the Institut National des Sciences de l'Univers of the Centre National de la Recherche Scientifique (CNRS) of France and the University of Hawaii. Based on observations collected at the European Southern Observatory under ESO programmes 097.D-0408 and 099.B-0384. Based in part on observations obtained at the Southern Astrophysical Research (SOAR) telescope, which is a joint project of the Ministério da Ciência, Tecnologia e Inovações (MCTI/LNA) do Brasil, the US National Science Foundation, NOIRLab, the University of North Carolina at Chapel Hill (UNC), and Michigan State University (MSU).

1. Introduction

Lenticular galaxies are an intermediate class of objects. Their physical, structural, and kinematical properties are between those of quiescent ellipticals and star-forming, rotating discs (Hubble 1936; van den Bergh 1976). They are generally rotation-supported systems (Dressler & Sandage 1983; Emsellem et al. 2011) composed of a prominent bulge with spectro-photometric properties similar to those of ellipticals and an extended disc similar to that of early-type spirals (Burstein 1979; Laurikainen et al. 2005; Erwin et al. 2015). They are composed of evolved stellar populations such as those dominating in early-type galaxies (Sandage & Visvanathan 1978a,b; Visvanathan & Sandage 1977), but can contain a significant quantity of cold atomic (van Driel & van Woerden 1991; Morganti et al. 2006; Serra et al. 2012) and molecular gas (Thronson et al. 1989; Sage & Wrobel 1989; Welch & Sage 2003; Davis et al. 2011, 2013; Young et al. 2011, 2014). They are preferentially located in dense regions such as groups and clusters (Dressler 1980; Whitmore et al. 1993; Dressler et al. 1997), suggesting that the environment might have played a major role in their evolution, but are also present in the field (Sandage & Visvanathan 1978b; Bamford et al. 2009). Their physical, structural, and kinematical properties also seem to vary as a function of their total mass, indicating that the evolutionary paths that gave birth to these objects can be complex and multiple (van den Bergh 1990; Erwin et al. 2012; Fraser-McKelvie et al. 2018).

Different scenarios have been proposed in the literature to explain the origin of lenticulars. They include internal secular evolution (e.g. Friedli & Martinet 1993; Laurikainen et al. 2006; Masters et al. 2010; Fraser-McKelvie et al. 2018; Rizzo et al. 2018), with an efficient gas ejection due to the feedback of an active galactic nucleus (AGN) (van den Bergh 2009), disc instabilities (Bournaud et al. 2007, 2011; Davis et al. 2014; Bournaud 2016), the fading of the star formation activity of late-type galaxies due to the lack of fresh infalling gas once they become satellites of a larger halo (starvation; Larson et al. 1980; Bekki et al. 2002), the quenching of the star formation activity of spiral galaxies in rich clusters once their gas content has been removed during the interaction with the surrounding hostile environment (e.g. Quilis et al. 2000; Burstein et al. 2005; Boselli & Gavazzi 2006, 2014; Boselli et al. 2021a), or more violent gravitational interactions (e.g. Byrd & Valtonen 1990; Dressler 2004; Bekki & Couch 2011), including galaxy harassment and minor and major merging events (e.g. Spitzer & Baade 1951; Moore et al. 1998; Bekki 1998; Poggianti et al. 2009; Wilman et al. 2009; Tapia et al. 2017; Diaz et al. 2018; Eliche-Moral et al. 2018; Méndez-Abreu et al. 2018; Davis et al. 2019). Finally, they can be the descendants of double-peak emission line galaxies, which is a peculiar population of objects that is observed at different redshifts (the interest in these objects has grown significantly in the past years; Domínguez Sánchez et al. 2018; Maschmann et al. 2020), of dusty starburst galaxies observed in intermediate-redshift clusters (e.g. Geach et al. 2009), or of E+A and post-starburst galaxies in clusters and in the field (Zabludoff et al. 1996; Poggianti et al. 1999, 2004; Yang et al. 2008).

Because a high fraction of lenticulars is located in local high-density environments but was much less frequent in similar structures at earlier epochs ($z \sim 0.5$, Dressler et al. 1997), the lenticulars may have been formed only recently. Local systems therefore probably still keep the imprints of their recent transformation in their physical, structural, and kinematical properties. Nearby clusters, in which most of these systems are now located (e.g. Dressler et al. 1997), are thus a unique laboratory in which to study the formation and evolution of these intriguing objects in detail. Their proximity enables a detailed analysis of the different galaxy components (stars, gas, and dust) at exquisite sensitivity and angular resolution on large, statistically significant samples spanning a wide range in stellar mass and galaxy density.

The Virgo Environmental Survey Tracing Ionised Gas Emission (VESTIGE) is a deep Hα narrow-band blind imaging survey of the Virgo cluster (Boselli et al. 2018a). This survey has been designed to identify galaxies undergoing a perturbation with the hostile surrounding environment (NGC 4254, NGC 4424, NGC 4569, and IC 3476; Boselli et al. 2016a, 2018b,c, 2021b; NGC 4330, Fossati et al. 2018; Vollmer et al. 2021; Sardaneta et al. 2022) and to understand its effects on the star formation process down to scales of individual HII regions (Boselli et al. 2020, 2021b). Because of its untargeted nature, the spectacular quality of the data in terms of sensitivity and angular resolution are an excellent tool for discovering objects with peculiar features in their ionised gas distribution (e.g. ionised gas filaments in M87; Boselli et al. 2019; dust within the tails of ram pressure stripped galaxies; Longobardi et al. 2020; ionised gas associated with an almost dark galaxy; Junais et al. 2021), which opens new exciting perspectives in the study of galaxy evolution in rich environments.

The VESTIGE survey, combined with the multifrequency data covering the entire electromagnetic spectrum available for the Virgo cluster region (A GALEX Ultraviolet Virgo Cluster Survey – GUViCS; Boselli et al. 2011; The Next Generation Virgo Cluster Survey – NGVS; Ferrarese et al. 2012; The *Herschel* Virgo Cluster Survey – HeViCS; Davies et al. 2010; The Arecibo Legacy Fast ALFA Survey – ALFALFA; Giovanelli et al. 2005) provides us with a unique opportunity to study a complete sample of lenticular galaxies in the closest cluster of galaxies in exquisite detail. The distance of the cluster (16.5 Mpc; Gavazzi et al. 1999; Mei et al. 2007) is 1 arcsec, which corresponds to 80 pc. This is a sufficiently low value to dissect the different galaxy components (stars, gas, and dust) down to small scales that cannot be reached elsewhere. The cluster, which is unrelaxed and thus includes objects that still undergo a transformation, is ideal for a detailed study of lenticular galaxies, which are numerous (78 catalogued in the Virgo Cluster Catalogue (VCC) as Virgo cluster members by Binggeli et al. 1985) and span a wide range in luminosity and stellar mass (e.g. Sandage et al. 1985).

During the survey, we discovered a number of these objects with peculiar features that indicate ionised gas in their inner regions. In this paper, we study the properties of a sample of eight massive ($10^{10} \lesssim M_{\rm star} \lesssim 10^{11}\,M_{\odot}$) lenticular galaxies with interesting features in the ionised gas distribution, such as discs or filaments. These types of features have been identified previously in the literature (e.g. Goudfrooij et al. 1994; Macchetto et al. 1996; Finkelman et al. 2010), but the quality of the data in terms of sensitivity and angular resolution, combined with an intense stellar continuum emission, hampered a detailed analysis of the properties of the emitting gas, the identification of the dominant ionising source, the study of its possible relation with star formation, and the ultimate understanding of their origin. Different questions related to the nature of these ionised gas features indeed remain unanswered. First, the ionisation source of the gas may be a central AGN, which is generally present in massive systems, or it may be stellar photoionisation

due to young stars, a cooling of the hot gas corona, or the general interstellar radiation field (ISRF) that is dominant in these evolved systems (e.g. Annibali et al. 2010; Panuzzo et al. 2011; Lagos et al. 2014). Second, if the source of ionisation is young stars, the gas may form stars at a similar rate as expected from the Kennicutt-Schmidt relation that is observed in normal star-forming late-type systems (e.g. Davis et al. 2014). This needs to be confirmed, however. Third, it is unclear whether the properties of the gas (gas-to-dust ratio, metallicity, etc.) are similar to those of the gaseous discs of normal star-forming late-type galaxies of comparable stellar mass (e.g. Davis et al. 2015). Finally, the origin of this gas is still not determined. It may be recently accreted gas, or residuals of a gas disc that was radially stripped outside-in by a recent episode of ram pressure, it may be gas produced by the mass loss of evolved stars, or even gas supplied by the radiative cooling of the galaxy hot haloes (e.g. Lagos et al. 2014).

A detailed analysis of the physical properties of the ionised gas emission of a statistically complete sample of lenticular galaxies in the Virgo cluster will be possible only after the VESTIGE survey is completed. Here we limit the analysis to a sample of eight objects with excellent data gathered at different frequencies, including medium-resolution integral field unit (IFU) spectroscopy gathered with the Multi Unit Spectroscopic Explorer (MUSE), high angular resolution *Hubble* Space Telescope (HST) imaging, ultraviolet (UV) (GALEX and ASTROSAT UltraViolet Imaging Telescope (UVIT)) and far-infrared (*Spitzer* and *Herschel*) imaging, and millimetric interferometry (Atacama Large Millimetre Array – ALMA, Combined Array for Research in Millimetre-wave Astronomy – CARMA). The paper is structured as follows: the sample is described in Sect. 2. The narrow-band VESTIGE observations, along with the new MUSE IFU and Southern Astrophysical Research (SOAR) long-slit spectroscopy, the ASTROSAT/UVIT and the ALMA observations and data reduction, and the other published multifrequency data analysed in this work are described in Sect. 3. In Sect. 4 we analyse the physical properties of the ionised gas and of the other galaxy components and discuss them in the framework of galaxy evolution in Sect. 5, which also includes our conclusion. A dedicated section describing each single object is given in Appendix A.

2. Sample

The sample analysed in this work is composed of eight massive ($10^{10} \lesssim M_{\rm star} \lesssim 10^{11}\,M_\odot$) S0-S0/a galaxies located within the inner regions of the Virgo cluster. In these locations, the VESTIGE survey has already reached a sufficient depth to detect low surface brightness features in the ionised gas component. For this reason, the sample is by no means complete. We recall, however, that out of the 78 lenticular galaxies (S0-S0/a) that were identified as Virgo cluster members by Binggeli et al. (1985) in the VCC, only 33 have a stellar mass $M_{\rm star} > 10^{10}\,M_\odot$. The 8 selected galaxies with ionised gas features analysed in this work correspond to ∼25% of the massive lenticulars in Virgo. The VESTIGE survey, which at the time of writing is still incomplete, covered only ∼60% of the VCC, and full depth is reached only over 25% of the cluster. The estimated detection rate of ∼25% should thus be considered as a lower limit, which makes these objects a representative population of the massive lenticulars of the cluster. These 8 galaxies were selected because they show some evident structured ionised gas emission in the deep continuum-subtracted images. These ionised gas features can either be low surface brightness filaments extending from the nucleus to the outer regions (NGC 4262 and 4552), discs (NGC 4429, 4459, 4476, 4477, and 4526), or both (NGC 4469). The main parameters of the observed galaxies, including those derived in this work, are given in Table 1.

3. Observations and data reduction

3.1. VESTIGE narrow-band imaging

Narrow-band (NB) Hα imaging observations were carried out during the VESTIGE survey (Boselli et al. 2018a). The data were obtained using MegaCam at the CFHT in the NB filter MP9603 (λ_c = 6590 Å; $\Delta\lambda$ = 104 Å). Because of the redshift of the galaxies, this filter includes the emission of the Balmer Hα line and of the two [NII] lines (λ = 6548, 6583 Å). Hereafter, we refer to the Hα+[NII] band simply as Hα, unless otherwise stated. Galaxies were observed with typically 1–2 h of integration in the NB filter and 7–12 min in the broad-band r filter. Observation in the r filter is necessary to subtract the stellar continuum (see Table 2). A detailed description of the observing strategy and of the data reduction is given in Boselli et al. (2018a). Briefly, MegaCam is composed of 40 CCDs with a pixel scale of 0.187 arcsec pixel^{-1}. The observations were carried out following a specific observing sequence to optimise the determination of the sky background, which is necessary to detect low surface brightness extended features. The observations were taken during excellent sky conditions, with a typical seeing ranging from 0.65 to 0.86 arcsec (see Table 2). The sensitivity of the survey at full depth (2 h in the NB filter, 12 min in the broad r-band filter) is $f(\mathrm{H}\alpha) \simeq 4 \times 10^{-17}$ erg s^{-1} cm^{-2} (5σ) for point sources and $\Sigma(\mathrm{H}\alpha) \simeq 2 \times 10^{-18}$ erg s^{-1} cm^{-2} arcsec^{-2} (1σ after smoothing the data to ∼3″ resolution) for extended sources.

As for all the VESTIGE data, the images were reduced using Elixir-LSB (Ferrarese et al. 2012). This is a data reduction pipeline designed to detect extended and low surface brightness features. The photometric calibration in both filters and the astrometric corrections were then secured using the standard MegaCam procedures as described in Gwyn (2008). The typical photometric uncertainty in both bands is $\lesssim$0.02–0.03 mag.

As extensively described in Boselli et al. (2019), the subtraction of the stellar continuum is particularly critical in early-type galaxies, in which the emission of the ionised gas is marginal with respect to that of the stars. We thus followed the same procedure as was used for M87, where the stellar continuum was derived using the r-band frame combined with a $g - r$ colour map, the latter constructed using the NGVS g-band frame. For this purpose, we used a particular g-band frame produced by the NGVS survey, where saturated pixels in the core of these bright galaxies were accurately replaced with those gathered during short exposures (Ferrarese et al. 2012). The continuum-subtracted Hα images of the eight galaxies analysed in this work are shown in Fig. 1. Table 1 gives the total fluxes (in units of erg s^{-1} cm^{-2}) and uncertainties of the Hα emission line of the eight target galaxies. As for the other VESTIGE papers (Fossati et al. 2018; Boselli et al. 2018b,c), fluxes and uncertainties were derived by measuring both the galaxy emission and the sky background within the same elliptical aperture, randomly displaced on the sky after masking other contaminating sources. To minimise the uncertainty on the sky determination, this procedure was run 1000 times. In a few galaxies (NGC 4262, 4459, 4526, and 4552), the r-band images are slightly saturated in the nucleus. For these objects, the saturated central region was masked. The uncertainties on the fluxes were obtained as the quadratic sum of the uncertainties on the

Table 1. Physical properties of the target galaxies.

Variable	Units	NGC 4262	Ref	NGC 4429	Ref.	NGC 4459	Ref	NGC 4469	Ref.
Type		SB(s)0–?	1	SA(r)0+;LINER, HII	1	SA(r)0+;HII, LINER	1	SB(s)0/a?sp;LINER	1
Spec. class.		Passive,Passive	2	– ,wAGN	2	–, Retired	2	Transition, wAGN	2
cz	km s^{-1}	1359	1	1104	1	1192	1	539	1
Distance	Mpc	16.5	4,5	16.5	4,5	16.5	4,5	23.0	5
Membership		Cluster A	5	Cluster A	5	Cluster A	5	Cluster B	5
Proj. distance from cluster core	kpc	1100	T.W.	440	T.W.	480	T.W.	300 [(a)]	T.W.
$R_{\rm eff}(i)$	kpc	0.60	6	3.21	6	2.86	6	2.87	6
Fast/slow rotator		F	7	F	7	F	7	–	
log $M_{\rm star}$ [(b)]	$M_\odot$	10.23 ± 0.03	T.W.	10.90 ± 0.02	T.W	10.81 ± 0.02	T.W.	10.65 ± 0.02	T.W.
log $M_{\rm dust}$	$M_\odot$	6.57 ± 0.87	T.W.	6.26 ± 0.07	T.W.	6.18 ± 0.03	T.W.	6.88 ± 0.02	T.W.
log M(HI)	$M_\odot$	8.75	8	<7.12	8	<6.93	8	7.64	9
log $M(H_2)$ [(c)]	$M_\odot$	8.47 ± 0.30	T.W.	8.62 ± 0.20	T.W.	8.68 ± 0.10	T.W.	8.79 ± 0.30	T.W.
log f(Hα + [NII])	erg s^{-1} cm^{-2}	-12.61 ± 0.30	T.W.	-12.67 ± 0.01	T.W.	-12.79 ± 0.01	T.W.	-12.62 ± 0.05	T.W.
log L(Hα)	erg s^{-1}	39.73 ± 0.30	T.W.	40.07 ± 0.04	T.W.	39.90 ± 0.21	T.W.	40.49 ± 0.05	T.W.
R(Hα)	kpc	10.73	T.W.	1.22	T.W.	1.05	T.W.	0.99[f]	T.W.
SFR	$M_\odot$ yr^{-1}	0.027 ± 0.019	T.W.	0.059 ± 0.005	T.W.	0.040 ± 0.019	T.W.	0.155 ± 0.019	T.W.
log Σ(SFR) [(d)]	$M_\odot$ yr^{-1}kpc^{-2}	-4.12 ± 0.30	T.W.	-1.90 ± 0.04	T.W.	-1.93 ± 0.21	T.W.	-1.30 ± 0.05	T.W.
Variable	Units	NGC 4476	Ref	NGC 4477	Ref	NGC4526	Ref	NGC4552	Ref
Type		SA(r)0–	1	SB(s)0:?, Sy2	1	SAB(s)0:	1	E;LINER,HII,Sy2	1
Spec. class.		Passive,–	3	AGN,wAGN	2	HII,wAGN	2	–,Retired	2
cz	km s^{-1}	1968	1	1338	1	448	1	340	1
Distance	Mpc	16.5	4,5	16.5	4,5	16.5	4,5	16.5	4,5
Membership		Cluster A	5	Cluster A	5	Virgo S. Ext.	5	Cluster A	5
Proj. distance from cluster core	kpc	60	T.W.	360	T.W.	1350	T.W.	350	T.W.
$R_{\rm eff}(i)$	kpc	1.26	6	2.56	6	4.73	6	3.32	6
Fast/slow rotator		S	7	F	7	F	7	S	7
log $M_{\rm star}$ [(b)]	$M_\odot$	10.00 ± 0.02	T.W.	10.71 ± 0.03	T.W.	11.07 ± 0.03	T.W.	10.99 ± 0.02	T.W.
log $M_{\rm dust}$	$M_\odot$	6.03 ± 0.06	T.W.	5.76 ± 0.09	T.W.	7.00 ± 0.07	T.W.	6.78 ± 0.28	T.W.
log M(HI)	$M_\odot$	–		<6.95	8	7.11	10	<6.91	8
log $M(H_2)$ [(c)]	$M_\odot$	8.17 ± 0.10	T.W.	7.25 ± 0.20	T.W.	8.50 ± 0.10	T.W.	8.68 ± 0.30	T.W.
log f(Hα + [NII])	erg s^{-1} cm^{-2}	-13.10 ± 0.01	T.W.	-12.45 ± 0.01	T.W.	-12.63 ± 0.01	T.W.	-12.56 ± 0.01	T.W.
log L(Hα) [(c)]	erg s^{-1}	39.69 ± 0.04	T.W.	39.93 ± 0.06	T.W.	40.47 ± 0.01	T.W.	40.05 ± 0.02	T.W.
R(Hα)	kpc	0.73	T.W.	2.04	T.W.	1.45	T.W.	1.78	T.W.
SFR [(b)]	$M_\odot$ yr^{-1}	0.025 ± 0.002	T.W.	0.042 ± 0.006	T.W.	0.148 ± 0.001	T.W.	0.057 ± 0.003	T.W.
log Σ(SFR) [(d)]	$M_\odot$ yr^{-1}kpc^{-2}	-1.83 ± 0.04	T.W.	-2.49 ± 0.06	T.W.	-1.65 ± 0.01	T.W.	-2.23 ± 0.02	T.W.

Notes. [(a)]For NGC 4469, distance from M49. [(b)]$M_{\rm star}$ and SFR are derived assuming a Chabrier (2003) IMF and the Kennicutt (1998a) calibration. [(c)]Whenever available, in order of priority: ALMA 12 m, CARMA, from dust mass using a constant gas-to-dust ratio $G/D = 80$, and assuming an uncertainty of 0.1, 0.2, and 0.3 dex, respectively. [(d)]Star formation rate surface density within $R(H\alpha)$.
References. (1) NED, (2) Gavazzi et al. (2018a) (BTP and WHAN classification), (3) Derived from the SDSS spectrum, (4) Mei et al. (2007), (5) Gavazzi et al. (1999), (6) NGVS, (7) Emsellem et al. (2011), (8) Serra et al. (2012), (9) Boselli et al. (2014a, 2010a,b), Haynes et al. (2018).

Table 2. VESTIGE observational properties of the target galaxies.

Name	Units	NGC 4262	NGC 4429	NGC 4459	NGC 4469
N. exposures		7	10	12	11
Seeing	arcsec	0.65	0.79	0.84	0.69
Name	Units	NGC 4476	NGC 4477	NGC 4526	NGC 4552
N. exposures		12	12	8	12
Seeing	arcsec	0.86	0.84	0.69	0.84

Notes. Each single exposure is 10 min in the Hα NB filter, and 1 min in the broad-band r filter.

flux counts and the uncertainties on the background (rms of the bootstrap iterations). The uncertainties on the flux counts were derived assuming a Poissonian distribution for the source photo-electrons. The extracted fluxes therefore give integrated values. With the exception of the two galaxies NGC 4262 and NGC 4552, in which the Hα emission is peaked in the centre, the extracted fluxes are representative of the discs of ionised gas.

3.2. ASTROSAT/UVIT imaging

Three of the target galaxies were observed with ASTROSAT/UVIT (Agrawal 2006; Tandon et al. 2020). One of them, NGC 4429, was observed in May 2020 using the far-UV (FUV) filter BaF2 (λ_c = 1541 Å; $\Delta\lambda$ = 380 Å) during a run dedicated to the observations of a representative sample of Virgo cluster galaxies (PI. J. Hutchings). The other

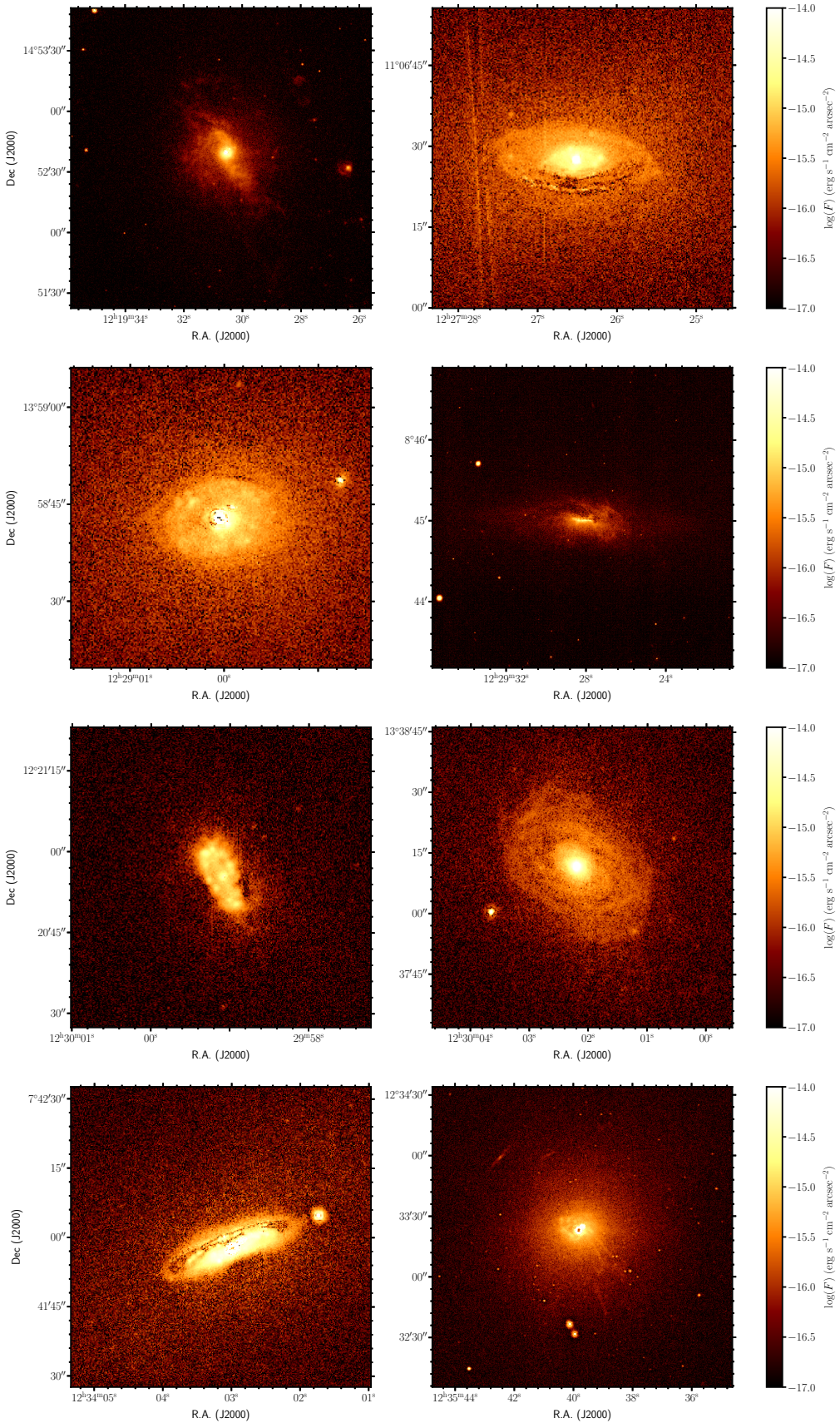

Fig. 1. Continuum-subtracted Hα images of the galaxies NGC 4262 (*first row, left*), 4429 (*first row, right*), 4459 (*second row, left*), 4469 (*second row, right*), 4476 (*third row, left*), 4477 (*third row, right*), 4526 (*last row, left*), and 4552 (*last row, right*). As in all the following figures, north is up, and east is to the left.

Table 3. ASTROSAT/UVIT data.

NGC units	Filter	Exp.time sec	Limiting S.B. mag arcsec^{-2}
4262	BaF2	2660	25.7
	Silica15	2747	26.5
4429	BaF2	7142	26.2
4476	BaF2	15896	27.1
	Silica15	15077	28.3

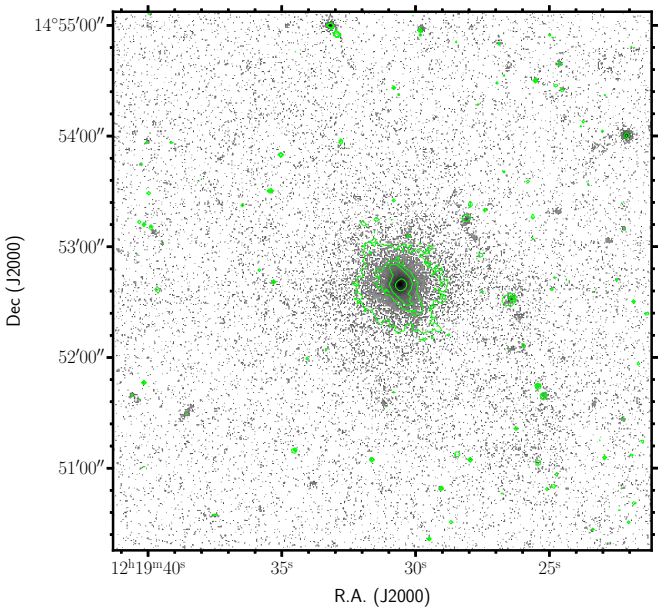

Fig. 2. Hα+[NII] contours (at a surface brightness level of Σ(Hα + [NII]) = 3×10^{-17}, 1×10^{-16}, 2×10^{-16}, 1×10^{-15} erg s^{-1} cm^{-2} arcsec^{-2}) plotted over the UVIT NUV image in the Silica15 band of the galaxy NGC 4262 (grey).

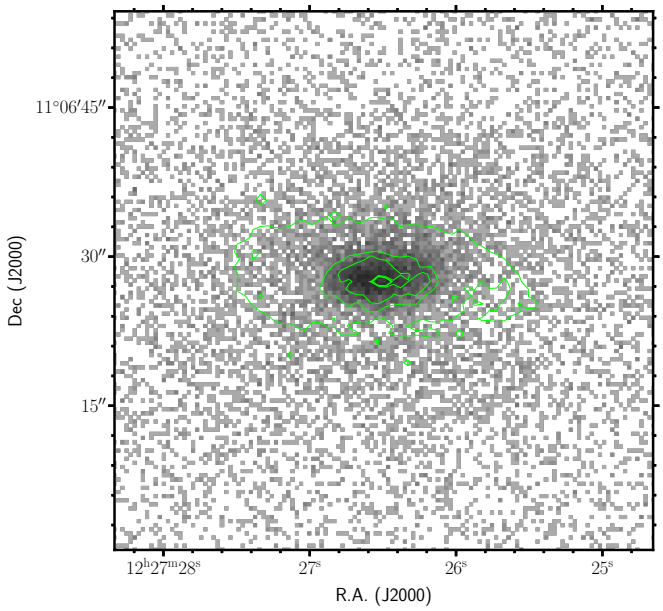

Fig. 3. Hα+[NII] contours (at a surface brightness level of Σ(Hα + [NII]) = 1.5×10^{-16}, 6×10^{-16}, 1.2×10^{-15} erg s^{-1} cm^{-2} arcsec^{-2}) plotted over the UVIT FUV image in the BaF2 band of the galaxy NGC 4429 (grey).

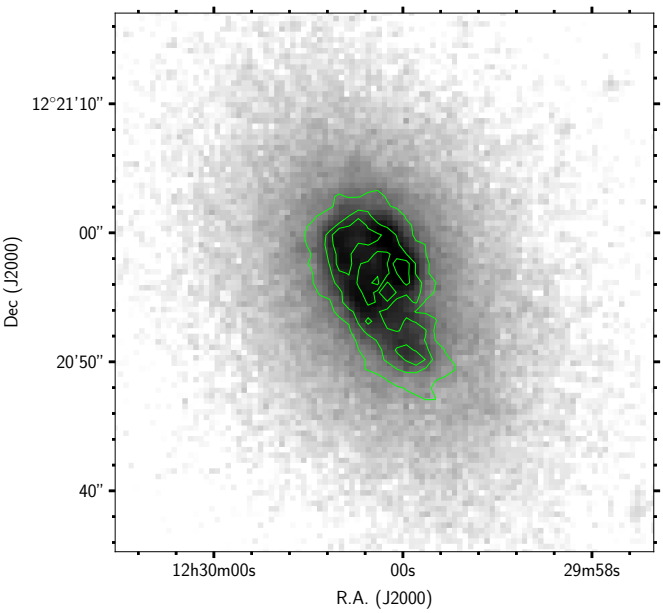

Fig. 4. Hα+[NII] contours (at a surface brightness level of Σ(Hα + [NII)] = 10^{-16}, 5×10^{-16}, 10^{-15} erg s^{-1} cm^{-2} arcsec^{-2}) plotted over the UVIT FUV image in the BaF2 band of the galaxy NGC 4476 (grey).

two galaxies, NGC 4262 and NGC 4476, were observed in the far-UV filter BaF2 and in the near-UV (NUV) filter Silica15 (λ_c = 2418 Å; $\Delta\lambda$ = 785 Å) and have data available in the archives, as specified in Table 3. The field of view of the instrument has a diameter of ≃28′ and an angular resolution of ≃1.5″. All the data were reduced following the prescriptions given in Tandon et al. (2020) using a zero-point of z_p = 17.771 mag for the FUV BaF2 filter and z_p = 19.763 for the NUV Silca15 filter. The astrometry was checked against the accurate NGVS data (Ferrarese et al. 2012, see below). The ASTROSAT/UVIT images of the three galaxies are shown in Figs. 2–4.

3.3. MUSE spectroscopy

Two of the galaxies, NGC 4469 and NGC 4526, were observed with MUSE during the 099.B-0384 (PI O. Gonzalez) and 097.D-0408 (PI J. Anderson) programs. The first program was designed to study the kinematics of boxy early-type discs, and the second program to study the properties of host galaxies of core-collapse supernovae (the AMUSING survey, Galbany et al. 2016). The MUSE data were acquired in May 2017 and in May 2016 in the wide-field mode under medium ($FWHM$ = 1.19″) and good seeing conditions ($FWHM$ = 0.91″) for NGC 4469 and NGC 4526, respectively. The data cover the spectral range 4800–9300 Å with a spectral resolution R ∼ 2600 (1.25 Å sampling per pixel), corresponding to a limiting velocity dispersion σ ∼ 50 km s^{-1} (see Boselli et al. 2021b). The data were acquired with an integration time of 2448 s (NGC 4469) and 2360 s (NGC 4526), which enables reaching a typical sensitivity to low surface brightness features at Hα of Σ(Hα) ≃ 4×10^{-18} erg s^{-1} cm^{-2} arcsec^{-2}. The data were reduced using ad hoc procedures developed within the team and presented in Fossati et al. (2016), Consolandi et al. (2017), and Boselli et al. (2018c, 2021b). The astrometry of the data cubes was registered on the VESTIGE image using point sources in the field. A com-

Table 4. SOAR data.

NGC	Position	Hβ	[OIII]λ5007	Hα	[NII]λ6583	[SII]λ6716	[SII]λ6731	S/N(Hα)	S/N(Hβ)	C(Hβ)
4429	W	0.16	0.05	1.00	0.84	0.20	0.21	20.19	2.19	1.16 ± 0.67
4429	E	0.01	0.00	1.00	1.06	0.24	0.20	16.82	0.60	4.78 ± 2.45
4476	NW	0.16	0.03	1.00	0.47	0.16	0.11	55.65	5.92	1.11 ± 0.25
4476	SE	0.11	0.02	1.00	0.53	0.19	0.15	53.66	3.31	1.72 ± 0.44

Notes. Fluxes are normalised to Hα; the orientation of the slit was E–W for NGC 4429 and SE–NW (31° from north, counter clockwise) for NGC 4476.

Table 5. CO data.

NGC	ALMA transition	Beam	I(CO)	$M(H_2)$	CARMA transition	Beam	I(CO)	$M(H_2)$
units		″×″	Jy km s^{-1}	$M_\odot$		″×″	Jy km s^{-1}	$M_\odot$
4429	CO(3–2)	0.18×0.15	52.70	4.15×10^8	CO(1-0)	4.69×3.73	64.66	1.58×10^8
4459	CO(2–1)	0.58×0.50	127.00	4.77×10^8	CO(1-0)	9.01×5.53	55.52	1.36×10^8
4459	CO(2–1)	6.64×4.99	103.90	3.90×10^8	CO(1-0)			
4476	CO(2–1)	0.74×0.55	39.15	1.47×10^8	CO(1-0)	8.29×5.66	29.25	7.14×10^7
4476	CO(2–1)	7.08×4.77	40.17	1.51×10^8	CO(1-0)			
4477					CO(1-0)	3.30×2.62	7.34	1.79×10^7
4526	CO(1–0)	1.14×0.76	128.60	3.14×10^8	CO(1-0)	4.99×3.84	166.10	4.06×10^8

Notes. $M(H_2)$ are derived assuming a standard CO-to-H_2 conversion factor $X_{CO} = 2.3 \times 10^{20}$ cm^{-2}/(K km s^{-1}) (Strong et al. 1988) and an intensity ratio CO(2–1)/CO(1–0) = $R_{21} = 0.65$ and CO(3–2)/CO(1–0) = $R_{31} = 0.31$ (Leroy et al. 2021).

parison of the flux of the Hα+[NII] emission line extracted from the MUSE data cubes with the one obtained from the VESTIGE NB image gives $f(\mathrm{H}\alpha+[\mathrm{NII}])_{\mathrm{VESTIGE}}/f(\mathrm{H}\alpha+[\mathrm{NII}])_{\mathrm{MUSE}} = 1.05$ for NGC 4469 and $f(\mathrm{H}\alpha + [\mathrm{NII}])_{\mathrm{VESTIGE}}/f(\mathrm{H}\alpha + [\mathrm{NII}])_{\mathrm{MUSE}} = 1.18$ for NGC 4526. This difference, which is significantly larger than that observed in star-forming galaxies such as NGC 4424 ($\lesssim$3.5%; Boselli et al. 2018c) and IC 3476 ($\lesssim$1%; Boselli et al. 2021b), probably arises because (a) the Hα emission principally originates in the inner regions, where the total flux in the NB filter is highly dominated by uncertainties in the stellar continuum emission, and (b) the Hα flux derived from the MUSE data was determined after subtraction of the stellar continuum emission using the GANDALF code. In this way, the Hα line in MUSE was corrected for any possible contamination due to a strong underlying Balmer absorption that is not taken into account in the NB imaging data of VESTIGE. The 5–18% differences (0.02–0.07 dex) observed in NGC 4469 and NGC 4526 can thus be considered as the typical uncertainty on the Hα flux determination on the NB VESTIGE data in these bright early-type systems. We recall, however, that 18% should be taken as an upper limit for the other galaxies, where the emission in their centre and the dust attenuation throughout the disc are less extreme than in NGC 4526.

3.4. SOAR spectroscopy

SOAR observations were carried out with the Goodman spectrograph (Clemens et al. 2004) on the 4.1 m Southern Astrophysical Research (SOAR) Telescope at Cerro Pachón on 14 April 2021. The spectra were taken with a 600 line mm^{-1} grating and a 1.5″wide slit, using a 2×2 binning, resulting in a spectral and spatial sampling of 1.3 Å pixel^{-1} and 0.3″pixel^{-1}, respectively. The resolving power of Goodman in the wavelength range 4350–7020 Å that is covered during the observations (MID configuration) is $R \simeq 2800$. The exposure time was 2.5 h (divided into five exposures of 1800 s) for NGC 4429 and 3 hr (divided into six exposures of 1800 s) for NGC 4476. Two spectrophotometric standard stars were observed, one at the beginning and one at the end of the night run, to secure the flux calibration.

The data were reduced with basic calibrations including bias, flat, cosmic ray removal, and wavelength calibration obtained using a combination of CuHeAr and HgArNe lamps. The standard star observations were reduced and the stellar spectrum was extracted and compared to the reference spectrum from the X-shooter calibration database to derive the instrument response function. The function was fit with a fourth-degree polynomial and applied to calibrate the science data, which were subsequently shifted and combined with mean statistics. To trace the properties of the Hα emitting disc and avoid any possible contamination from the nucleus, a pair of 1D spectra were extracted on either side of the spectral slit at radial distances from the galaxy centres of 3.″3–7.″5 and 3.″3–7.″8 for NGC 4429 and NGC 4476, respectively. Each spectrum was fit with the GANDALF code (Sarzi et al. 2006) using the MILES stellar spectral library (Vazdekis et al. 2010) to model the stellar continuum and the nebular line emission. Emission line fluxes, reported in Table 4, were averaged from the two spectral extractions when used in the following analysis.

3.5. ALMA

High-quality millimetric data necessary for the determination of the molecular gas content and distribution were gathered using ALMA and are available in the archives for the galaxies NGC 4429, 4459, 4476, and 4526 at different frequencies, as indicated in Table 5. NGC 4429 was observed during ALMA Cycle 1 (Project 2013.1.00493.S, PI M. Bureau) with 42 antennas in band 7 tuned between 343.5 GHz and 345.5 GHz, targeting the ^{12}CO(3–2) line. The spatial resolution was 0.19 × 0.16 arcsec. The observations were taken on 26 and 27 June

Table 6. Multiwavelength data of the target galaxies.

Galaxy	X-rays	Ref	UV	Ref	Visible	Ref
4262	*Chandra*	1	GALEX, UVIT	8,9,TW	CFHT, HST	10,11,TW
4429	*Chandra*	1	GALEX, UVIT	9,TW	CFHT, HST	11,12,TW
4459	*Chandra*, XMM	1,2	GALEX	9	CFHT, HST	10,11,TW
4469	*Chandra*	1	GALEX	9	CFHT, HST	11,TW
4476	*Chandra*, XMM	1,2	GALEX, UVIT	9,TW	CFHT, HST	10,11,TW
4477	*Chandra*, XMM	2,3,4	GALEX	9	CFHT, HST	11,TW
4526	*Chandra*, XMM	2,4	GALEX	9	CFHT, HST	10,11,TW
4552	*Chandra*, XMM	4,5,6,7	GALEX	9	CFHT, HST	10,11,TW
Galaxy	IR	Ref	CO	Ref	HI	Ref
4262	WISE, *Spitzer*, *Herschel*	13,13,15,16	IRAM	18	WSRT	24,25
4429	WISE, *Spitzer*, *Herschel*	13,13,15,16	CARMA, ALMA	12,19	WSRT	26
4459	WISE, *Spitzer*, *Herschel*	13,13,15,16	CARMA, ALMA, IRAM	18,21,TW	WSRT	26
4469	WISE, *Spitzer*, *Herschel*	13,13,15,16			Arecibo	27
4476	WISE, *Spitzer*, *Herschel*	13,17,TW	CARMA, ALMA	21,TW	WSRT	26
4477	WISE, *Spitzer*, *Herschel*	13,13,15,16	CARMA, PdBI, IRAM	18,22	WSRT	26
4526	WISE, *Spitzer*, *Herschel*	13,13,15,16	CARMA, ALMA, IRAM	18,23,TW	Arecibo	27
4552	WISE, *Spitzer*, *Herschel*	13,13,15,16	IRAM	18	WSRT	26

References. (1) *Chandra* data archive (P.Is.: Treu, Soria, Ptak, Gultekin); (2) XMM data archive (P.Is.: David, Forman, Sanders, Jansen, Boehringer, Turner, Aschenbach, Irwin); (3) Li et al. (2018); (4) Kim et al. (2019); (5) Machacek et al. (2006a); (6) Machacek et al. (2006b); (7) Kraft et al. (2017); (8) Bettoni et al. (2010); (9) Boselli et al. (2011); (10) Côté et al. (2004); (11) Ferrarese et al. (2012); (12) Davis et al. (2018); (13) Wright et al. (2010); (14) Bendo et al. (2012a); (15) Cortese et al. (2014); (16) Ciesla et al. (2012); (17) Auld et al. (2013); (18) Combes et al. (2007); (19) Alatalo et al. (2013); (20) Young et al. (2008); (21) Young (2002); (22) Crocker et al. (2011); (23) Utomo et al. (2015); (24) Krumm et al. (1985); (25) Oosterloo et al. (2010); (26) Serra et al. (2012); (27) Haynes et al. (2018).

2015 with a total integration time of 4233 s. The observations for NGC 4459 and NGC 4476 were carried out in Cycle 5 in September 2017 with a total integration time of ∼25 200 s using the 12 m and 7 m arrays (PI: M. Chevance; programme ID: 2017.1.00766.S). The spectral setup was optimised for the ^{12}CO(2–1) transition line in band 6 at 229.68 GHz rest frequency. At this frequency, the beam size for NGC 4459 was $0.58'' \times 0.50''$for the 12 m array and $6.64'' \times 4.99''$for 7 m array, while for NGC 4476, it was $0.744'' \times 0.555''$and $7.08'' \times 4.77''$for the 12 m and 7 m arrays, respectively. The observations for NGC 4526 were carried out in Cycle 6 in April 2019 with an integration time of 2580 seconds using the 12 m array (PI: S. Raimundo; programme ID: 2018.1.01599.S). The spectral setup was optimised for the ^{12}CO(1–0) transition line in band 6 at 114.96 GHz rest frequency, with a beam size of $1.14'' \times 0.76''$at a position angle of PA = −78.828°.

The original raw data were recalibrated with the Common Astronomy Software Applications package (CASA, McMullin et al. 2007), version 4.2.0, and re-imaged with the 5.8 version. The image reconstruction was performed using the standard TCLEAN deconvolution using the Briggs weighting algorithm (robust parameter 0.5). The moments were computed in CASA using a mask to cover all pixels below a given threshold to decrease the contribution of noise to the final maps, using the CASA task IMMOMENT.

3.6. Multifrequency data

The eight galaxies analysed in this work are all bright objects, most of which were targets of previous dedicated studies. For these galaxies, a large amount of multifrequency data is available that span the whole electromagnetic spectrum. The data come from a number of untageted surveys of the cluster in the visible (NGVS, Ferrarese et al. 2012, see Fig. 5), in the UV (GUViCS, Boselli et al. 2011), and in the far-infrared (HeViCS, Davies et al. 2010), or from dedicated observations, as summarised in Table 6. Data from targeted observations are also available: seven out of eight galaxies are included in the *Herschel* Reference Survey (HRS, Boselli et al. 2010a), with data available on the HeDam database[1]. Of particular interest for the present study are the HST images of the inner regions (see Fig. 6) taken during the Advanced Camera for Surveys (ACS) Virgo cluster survey (Côté et al. 2004) or in other targeted observations, which are available in the HST archive. Mid- and far-IR data in the Wide-field Infrared Survey Explorer (WISE, Wright et al. 2010) and Multiband Imaging Photometer for *Spitzer* (MIPS, Rieke et al. 2004) bands, necessary for an accurate dust attenuation correction and for the determination of the total dust content of the target galaxies, are available from Bendo et al. (2012a), Ciesla et al. (2014), and Boselli et al. (2014a). The IFU spectroscopic data gathered by the ATLAS^{3D} survey of Cappellari et al. (2011) are also relevant for our study. Finally, ^{12}CO(1–0) interferometric data obtained using the CARMA radiotelescope at an angular resolution significantly coarser than that reached by ALMA are available for five galaxies, as illustrated in Table 5. These data have been taken during the molecular gas survey of nearby early-type galaxies conducted by Alatalo et al. (2013). A few other objects have pointed observations taken with the Institut of Radio Astronomy (IRAM) radiotelescope (Combes et al. 2007). Six of these galaxies have also been observed at 21 cm with the WSRT during the HI follow-up of the ATLAS^{3D} sample, but only one of them has been detected (Serra et al. 2012). Finally, X-ray data from *Chandra* or XMM are available for all galaxies of the sample (see Table 6). Although these X-ray data are available, they are not always relevant for the present work. We refer to dedicated works when X-ray data are of interest for the following analysis.

[1] https://hedam.lam.fr/HRS/

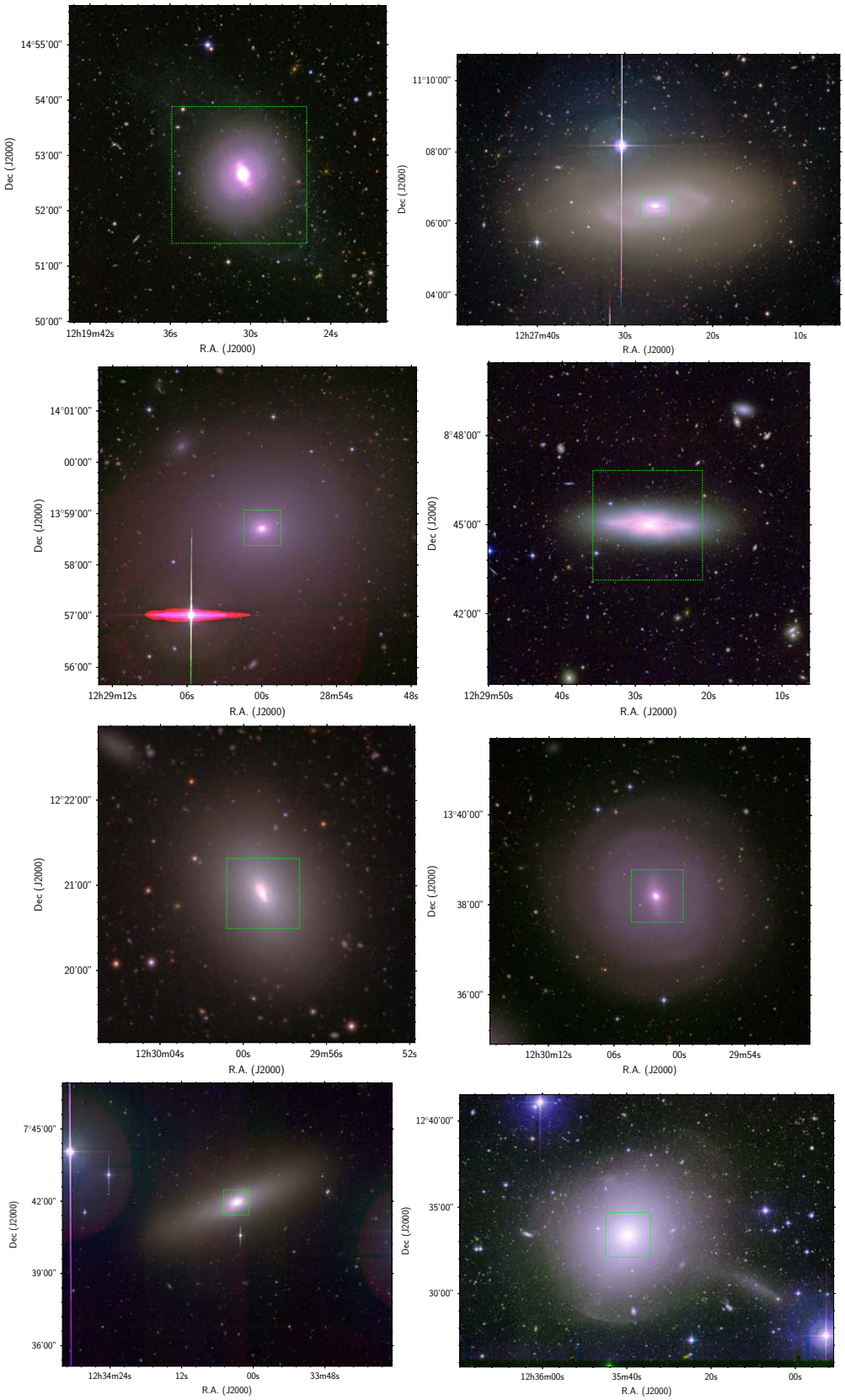

Fig. 5. Pseudo-colour images of the galaxies NGC 4262 (*first row, left*), 4429 (*first row, right*), 4459 (*second row, left*), 4469 (*second row, right*), 4476 (*third row, left*), 4477 (*third row, right*), 4526 (*last row, left*), and 4552 (*last row, right*) obtained combining the NGVS (Ferrarese et al. 2012) optical u and g in the blue channel, the r and NB in the green, and the i and the continuum-subtracted Hα in the red. The dashed green inset indicates the footprint of the continuum-subtracted Hα images shown in Fig. 1. At the assumed distance of the galaxies (16.5 Mpc), 1 arcmin = 4.8 kpc.

4. Physical parameters

4.1. Physical properties of the ionised gas

The excellent quality of the VESTIGE data allows us to use the Hα emission and distribution to derive several physical quantities of the ionised gas. These quantities are useful for the study of these intriguing objects.

4.1.1. Hα emission

Figure 1 shows the Hα continuum-subtracted images of the eight lenticular galaxies analysed in this work. In the very inner regions of five of them (NGC 4429, 4459, 4476, 4477, and 4526), an ionised gas disc with a size ($0.7 \lesssim R(\mathrm{H}\alpha) \lesssim 2.0$ kpc) is located. This is significantly smaller than that of the stellar component (Pogge & Eskridge 1993). The typical radial extent of the discs is ≃7–22% that of the stellar disc (isophotal radius in the i band as measured from the NGVS images) and their typical surface brightness is $2.4 \times 10^{-16} \lesssim \Sigma(\mathrm{H}\alpha) \lesssim 6.8 \times 10^{-16}$ erg s^{-1} cm^{-2} arcsec^{-2}. This is comparable to that of star-forming discs in late-type systems. All images show the presence of resolved, compact regions from the centre to the periphery of the discs. Tight, low surface brightness spiral arms are also visible in NGC 4477. The galaxies NGC 4262 and NGC 4552 show a rather more diffuse and filamentary distribution of the ionised gas similar to that observed in cooling flows associated with bright elliptical galaxies in the centre of rich clusters (Trinchieri & di Serego Alighieri 1991; Conselice et al. 2001; McDonald et al. 2010; Gavazzi et al. 2000; Boselli et al. 2019). These filaments have a relatively low surface brightness ($\Sigma(\mathrm{H}\alpha) \lesssim 10^{-16}$ erg s^{-1} cm^{-2} arcsec^{-2}), but do not extend outside the stellar component. Two unfolded, low surface brightness spiral arms and a few compact HII regions located along the ring structure seen in the UV by Bettoni et al. (2010) at the western side of the galaxy are also present in NGC 4262. The remaining boxy edge-on galaxy NGC 4469 has intermediate properties, with a very thin (≃100 pc) well-defined circumnuclear disc with a size of ≃400 pc in radius, and with filamentary structures extending up to ≃1 kpc from the plane of the galaxy, which is seen edge-on. The most extended of these structures extend from the western and eastern edges of the stellar disc in the southern direction (see Fig. 7). The eastern filament, which has a typical surface brightness of $\Sigma(\mathrm{H}\alpha) \simeq 2 \times 10^{-18}$ erg s^{-1} cm^{-2} arcsec^{-2} and is thus at the detection limit of the survey, extends out to ≃25 kpc in projected distance.

4.1.2. Balmer decrement and gas density

Spectroscopic data can be used to derive other physical properties of the ionised gas. Figure 8 shows the distribution of the Balmer decrement in the two galaxies NGC 4469 and NGC 4526, which reaches values up to Hα/H$\beta \simeq$ 6–8 in the inner discs, corresponding to $A(\mathrm{H}\alpha) \simeq$ 2–2.5 mag. These dust features seen in the Balmer decrement correspond fairly well to those observed in absorption in the VESTIGE NB images. Comparable values ($A(\mathrm{H}\alpha) \simeq 2.5$ mag) are derived using the SOAR data in NGC 4429 and NGC 4476, although these estimates are very uncertain because of the very low S/N in the Hβ line. Figure 9 shows the distribution of the [SII]λ6716 Å/[SII]λ6731 Å in the ionised gas disc of NGC 4469 and NGC 4526 derived from the MUSE data. Figure 9 shows that in NGC 4469, the doublet ratio is [SII]λ6716 Å/[SII]λ6731 Å ≃ 1.2–1.4 (corresponding to $n_\mathrm{e} \simeq$ 50–200 cm^{-3}; Osterbrock & Ferland 2006; Proxauf et al. 2014), as generally observed in late-type systems. In NGC 4526, [SII]λ6716 Å/[SII]λ6731 Å ≃ 1.2–1.3 (corresponding to $n_\mathrm{e} \simeq$ 100–200 cm^{-3}) along the dusty structure crossing the ionised gas disc from west to east of the galaxy and located north of its nucleus, where most of the dust is seen in absorption (see Fig. 6). In the rest of the disc, the ratio drops to [SII]λ6716 Å/[SII]λ6731 Å ≃ 0.9–1.0, corresponding to gas densities $n_\mathrm{e} \simeq$ 400–600 cm^{-3}. These gas densities are significantly higher than those generally encountered in normal star-forming late-type galaxies ($n_\mathrm{e} \simeq 50$ cm^{-3}; e.g. Rousseau-Nepton et al. 2018), including perturbed objects within the Virgo cluster (Boselli et al. 2021b). Similar values are derived for the discs of NGC 4429 ([SII]λ6716Å/[SII]λ6731 Å ≃ 1.1, corresponding to $n_e \simeq 300$ cm^{-3}) and NGC 4476 ([SII]λ6716 Å/[SII]λ6731 Å ≃ 1.4, corresponding to $n_\mathrm{e} \simeq$ 10–100 cm^{-3}) using the SOAR data.

4.1.3. Oxygen abundance

The MUSE data can also be used to trace the oxygen abundance distribution within the ionised gas disc of NGC 4469 and NGC 4526 (Fig. 10). For this purpose, we used the calibration of Curti et al. (2017) based on the Hβ, [OIII], [NII], and Hα lines with an $S/N > 5$. Figure 10 indicates that the ionised gas disc of NGC 4469 is metal rich in particular at its edges, where it reaches 12+log O/H ≃ 8.75–8.80, and slightly lower in its diffuse component (12+log O/H ≃ 8.70). NGC 4526 is also metal rich, with oxygen abundances $8.70 \lesssim$ 12+log O/H $\lesssim 8.80$. The higher values present in the dusty structure cross the galaxy from west to east north of the nucleus. This is also visible in absorption in the HST image (Fig. 6).

4.2. Source of ionisation

All sample galaxies are massive ($M_\mathrm{star} > 10^{10}\,M_\odot$) objects. Most of them are characterised by a weak or strong nuclear activity (see Table 1). Some of them also have an intense X-ray nuclear emission (NGC 4477, NGC 4526, and NGC 4552; Kim et al. 2019). It is thus possible that the observed gas, which is located in the innermost regions, is ionised by the nuclear activity. Being quiescent systems dominated by old stellar populations, the gas can also be ionised by evolved stars (e.g. Sarzi et al. 2010). There is, however, convincing evidence that at least in some of these objects, the Hα emitting gas is photoionised by young stars, and it is thus related to ongoing star formation activity. The first evidence comes from the spectroscopic data of NGC 4469 and NGC 4526 gathered with MUSE, which allow us to construct 2D diagnostic diagrams (Figs. 11 and 12).

Figure 11 clearly shows that in NGC 4469, the gas within the thin disc is photoionised by young stars, while the diffuse gas surrounding the disc in the z-direction is excited by a high-energy source. The line ratios consistently show that all this diffuse gas lies below the Seyfert/Low-ionisation nuclear emission-line (LINER) demarcation limit (Sharp & Bland-Hawthorn 2010), indicating that the gas might be shock-ionised. A similar, although less extreme, behaviour is observed in NGC 4526 (Fig. 12), with a possible exception in the nucleus. AGN or shock-type features in the BPT diagrams have been observed in the periphery of the disc in a few star-forming galaxies undergoing an external perturbation induced by the hostile surrounding cluster environment (ram pressure stripping in NGC 4424; Boselli et al. 2018c; CGCG 097-120;

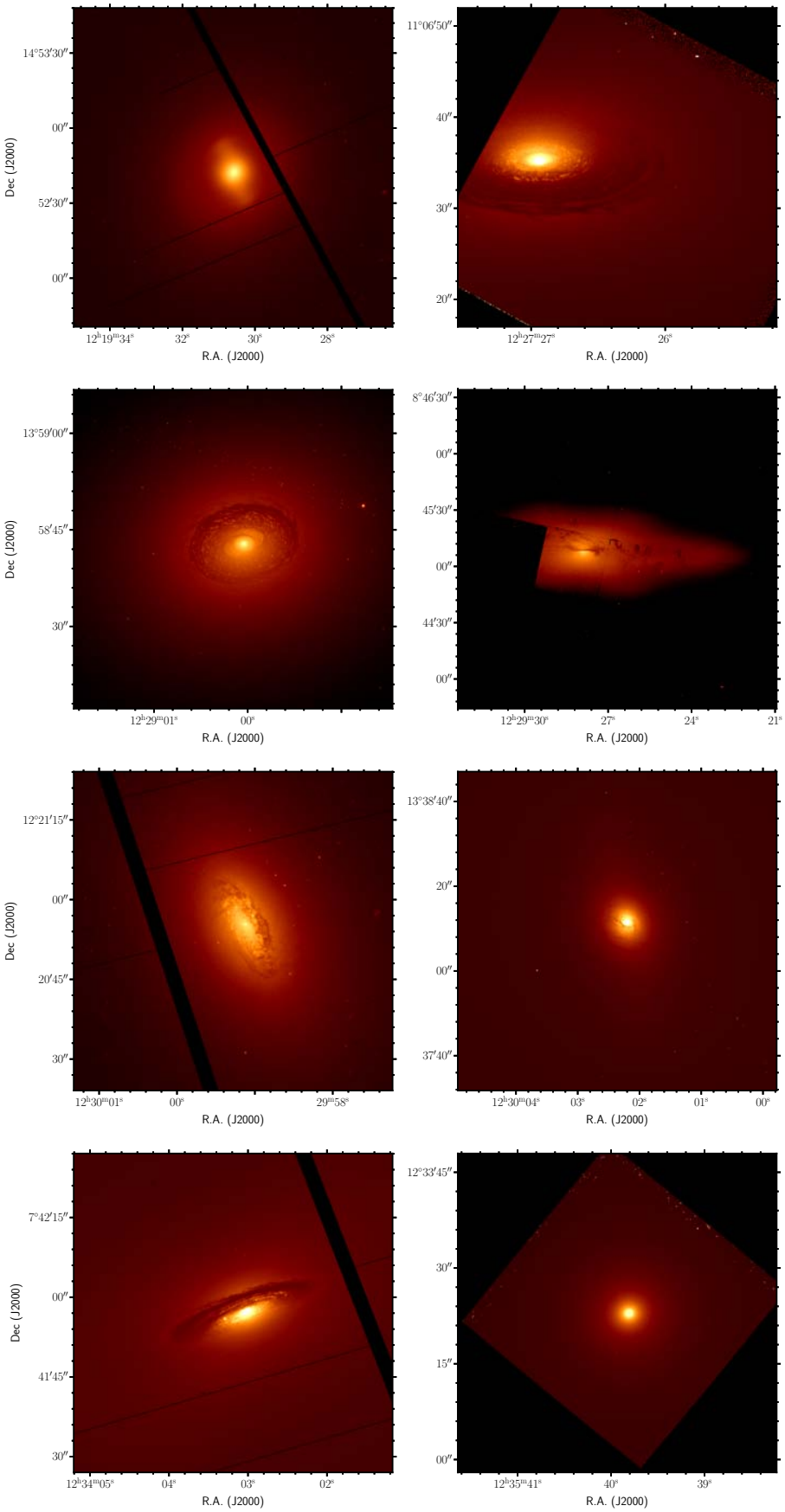

Fig. 6. HST images of the galaxies NGC 4262 (*F475W*; *first row, left*), 4429 (*F606W*; *first row, right*), 4459 (*F475W*; *second row, left*), 4469 (*F606W*; *second row, right*), 4476 (*F475W*; *third row, left*), 4477 (*F475W*; *third row, right*), 4526 (*F475W*; *last row, left*), and 4552 (*F555W*; *last row, right*).

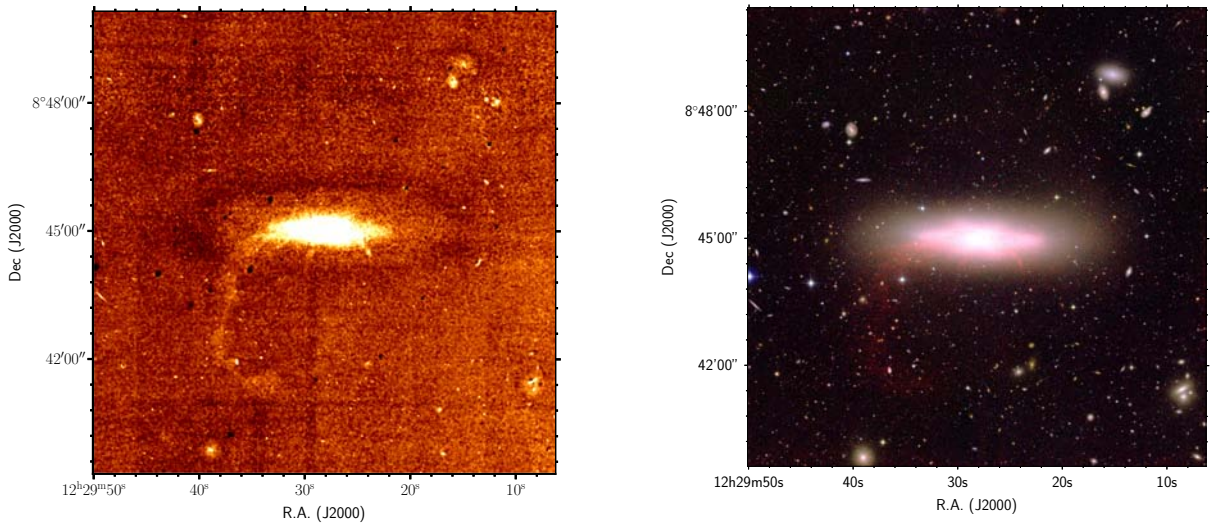

Fig. 7. Low-surface brightness and extended Hα emission of NGC 4469. *Left*: continuum-subtracted Hα image of the galaxy NGC 4469 smoothed to a resolution of 2.8″. The colour scale is arbitrarily chosen to highlight the low surface brightness tail of ionised gas at the SE of the galaxy disc. *Right*: pseudo-colour image obtained by combining the NGVS (Ferrarese et al. 2012) optical *u* and *g* in the blue channel, the *r* and NB in the green channel, and the *i* and the continuum-subtracted Hα image (this last smoothed to a resolution of 2.8″) in the red channel.

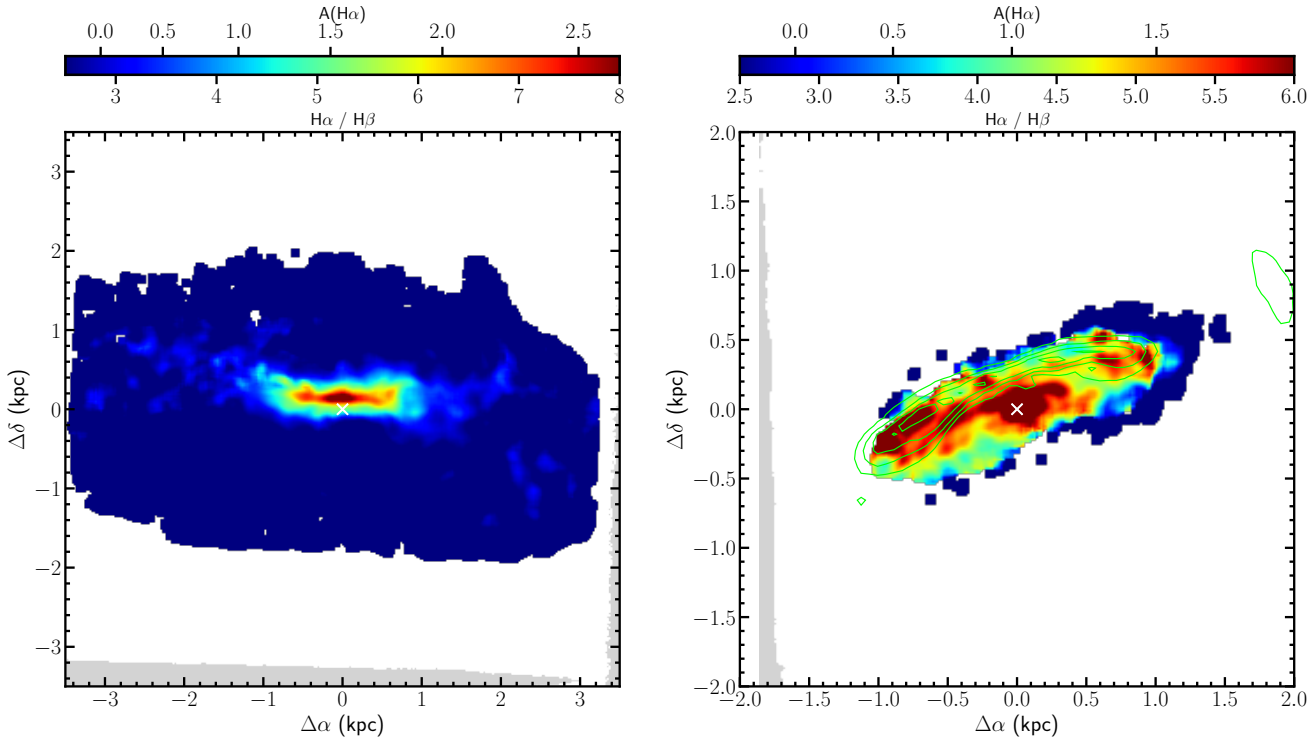

Fig. 8. Distribution of the Balmer decrement derived using the Hβ and Hα lines with an $S/N > 5$ extracted from the MUSE data in the galaxies NGC 4469 (*left*) and NGC 4526 (*right*). The white crosses show the position of the photometric centre. The green contours in NGC 4526 indicate A_g = 0.1, 0.3, 0.5, and 0.7 mag attenuation derived from the *g*-band NGVS image, as described in Sect. 4.4.

Fossati et al. 2019). We recall that although the presence of an AGN is not indicated by spectroscopic data (Figs. 11 and 12; see also Ho et al. 1997), NGC 4526 has a relatively strong X-ray point source in the nucleus that might be associated with a hidden AGN (Kim et al. 2019). Moreover, the BPT diagrams of NGC 4469 and NGC 4526 are different from those generally encountered in cooling-flow galaxies with ionised gas filaments, which rather suggest ionisation by a combination of slow shocks and star formation (McDonald et al. 2012).

A complete and homogeneous set of IFU data is unfortunately not available for the other galaxies. The extremely uncertain measure of the highly attenuated [OIII]λ5007 Å line prevents us from using the SOAR data to construct the same BPT diagrams for the galaxies NGC 4429 and NGC 4476. Their [NII]λ6583 Å/Hα ($\simeq$0.95 and $\simeq$0.50 for NGC 4429 and NGC 4476, respectively) and [SII]$\lambda\lambda$6716,6731 Å/Hα ($\simeq$0.85 and 0.61) and the [OIII]λ5007 Å/Hβ derived from the ATLAS^{3D} IFU spectroscopic data (see below) indicate that the properties

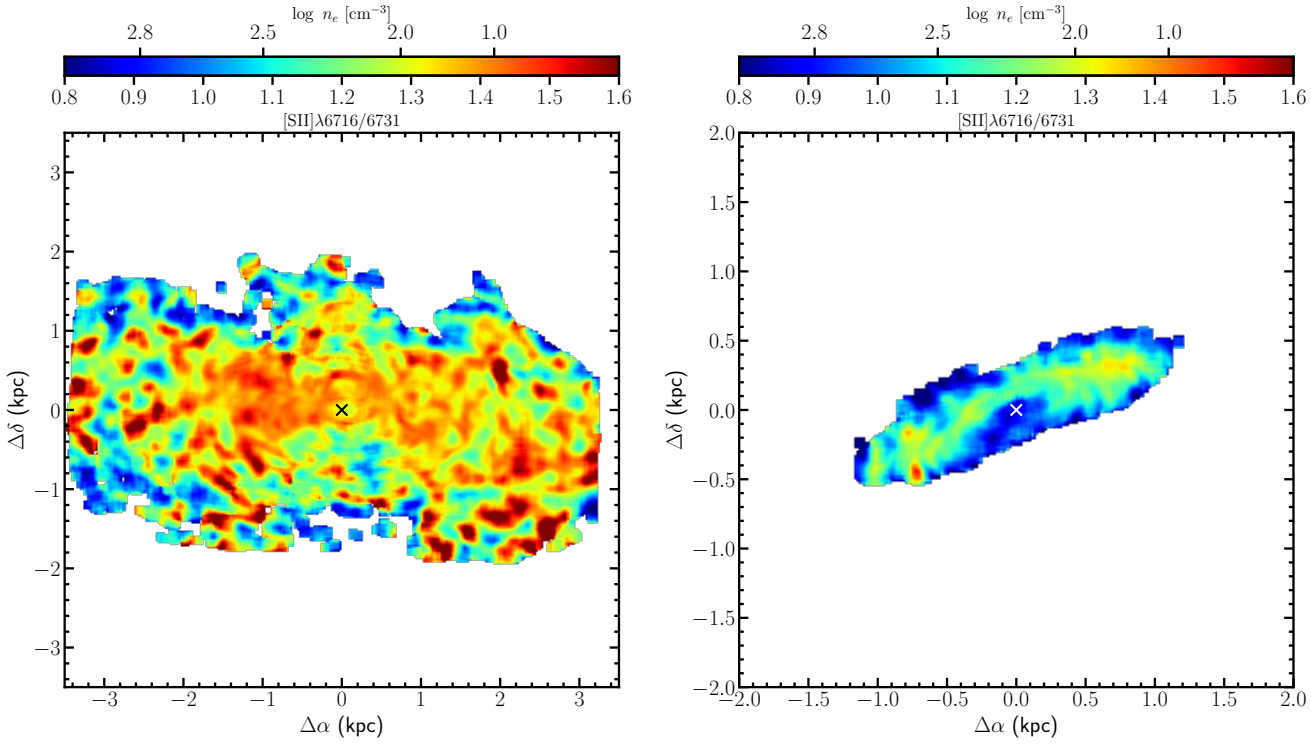

Fig. 9. Distribution of the [SII]λ6716 Å/[SII]λ6731 Å ratio for emission lines with an $S/N > 5$ extracted from the MUSE data of the galaxies NGC 4469 (*left*) and NGC 4526 (*right*). The black and white crosses show the position of the photometric centre.

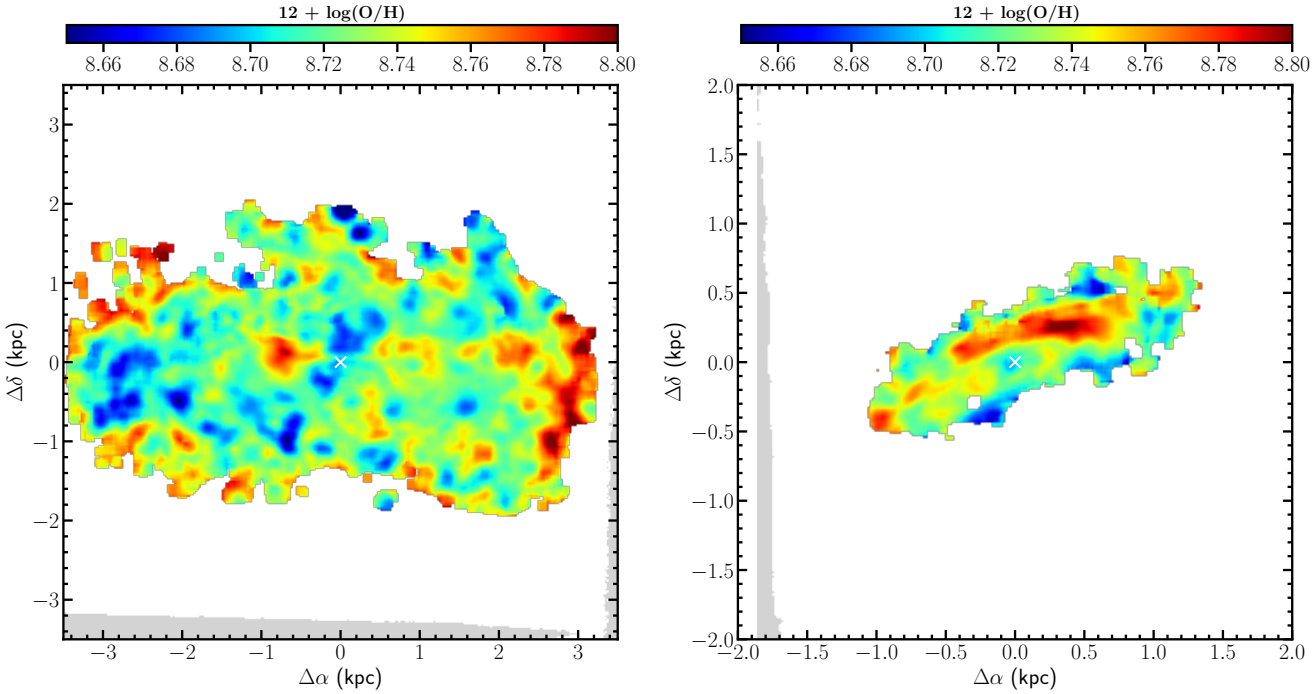

Fig. 10. Distribution of the metallicity derived using the calibration of Curti et al. (2017) using the Hβ, [OIII], [NII], and Hα lines with an $S/N > 5$ from the MUSE data for the galaxies NGC 4469 (*left*) and NGC 4526 (*right*). The white cross shows the position of the photometric centre.

of their ionised gas discs are similar to those encountered in NGC 4469 and NGC 4526. Integrated spectra in the optical domain (3700–7000 Å, $R \sim 1000$) obtained by drifting the slit of the spectrograph over the disc of the galaxies are available for the remaining objects from Gavazzi et al. (2004) and Boselli et al. (2013), but the sensitivity of the instrument and the small size of the telescope prevent the detection of the faint ionised gas. IFU data in the blue spectral domain (4800–5380 Å) are available from the ATLAS^{3D} survey (Cappellari et al. 2011). For an accurate analysis of the ionised gas properties of the full ATLAS^{3D} sample, we refer to Sarzi et al. (2010). The spectral coverage is not sufficient to construct BPT diagrams, but

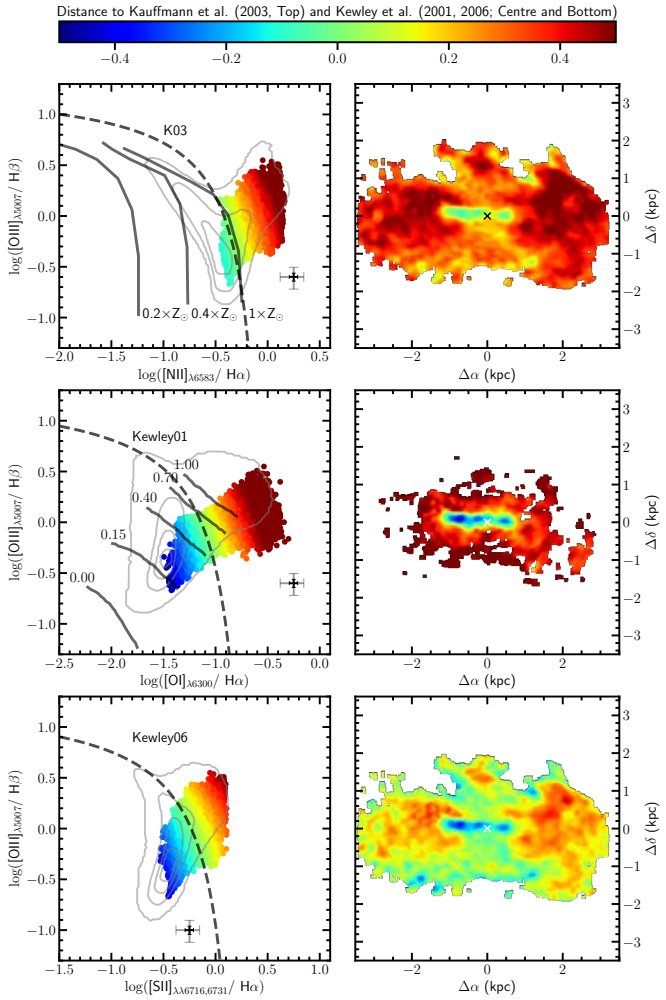

Fig. 11. 2D diagnostic diagarms. *Left*: [OIII]/Hβ vs. [NII]/Hα (*top*), [OIII]/Hβ vs. [OI]/Hα (*centre*), and [OIII]/Hβ vs. [SII]/Hα (*bottom*) BPT diagrams for emission lines with an $S/N > 5$ in the galaxy NGC 4469. The dashed curves separate AGN from HII regions (Kauffmann et al. 2003; Kewley et al. 2001, 2006). Data are colour-coded according to their minimum distance from these curves. The black and grey crosses indicate the typical error on the data for lines with $S/N \simeq 15$ and $S/N \simeq 5$, respectively. The grey contours show the distribution of a random sample of nuclear spectra of SDSS galaxies in the redshift range 0.01–0.1 and stellar masses $10^9 \leq M_{\rm star} \leq 10^{11}\,M_\odot$. The thick solid lines in the *upper left panel* show three different photoionisation models at different metallicities (0.2, 0.4, and 1 $Z_\odot$; Kewley et al. 2001). The lines in the middle left panel show the shock models of Rich et al. (2011) for increasing shock fractions (*from left to right*) in a twice-solar gas. *Right*: map of the spaxel distribution colour-coded according to their position in the BPT diagram. The black and white crosses indicate the position of the photometric centre of the galaxy.

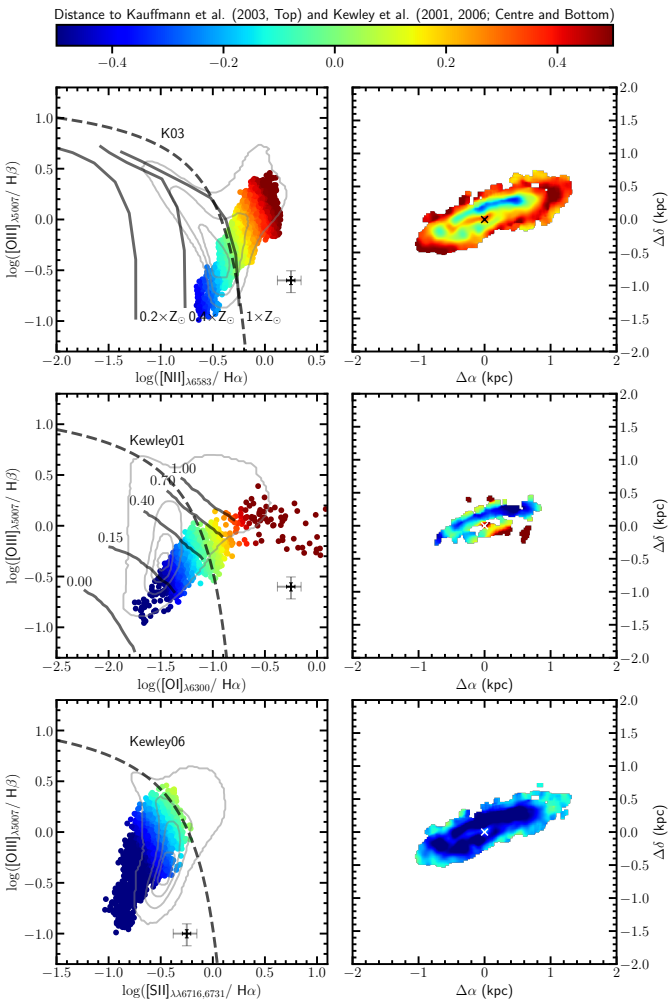

Fig. 12. Same as Fig. 11 for the galaxy NGC 4526.

it allows us to measure the mean [OIII]λ5007 Å/Hβ ratio in the inner 33×41 arcsec^2 of seven of the eight target galaxies. The mean values of the ratio derived after excluding all pixels included in the central 1 arcsec radius circle, which might be contaminated by a possible AGN activity, are given in Table 7. High values of [OIII]λ5007 Å/Hβ, which might suggest a high-ionisation source, are encountered in NGC 4262 ([OIII]λ5007 Å/Hβ = 2.16 ± 0.83), and with less extreme values in NGC 4477 ([OIII]λ5007 Å/Hβ = 1.51 ± 0.62) and NGC 4552 ([OIII]λ5007 Å/Hβ = 1.42 ± 0.71). For comparison, the ratio

Table 7. [OIII]λ5007 Å/Hβ ratios.

NGC	[OIII]λ5007 Å/Hβ	Ref.
4262	2.16 ± 0.83	1
4429	0.77 ± 0.39	1
4459	0.76 ± 0.37	1
4469 [(a)]	0.77 ± 0.28	2
4476	0.59 ± 0.25	1
4477	1.51 ± 0.62	1
4526	0.96 ± 0.57, 0.78 ± 0.42	1,2
4552	1.42 ± 0.71	1

Notes. $\pm$ gives the dispersion in the distribution. [(a)]the ratio is measured within the disc, excluding the diffuse extraplanar filaments, where the ratio is significantly higher: [OIII]λ5007 Å/Hβ = 1.19 ± 0.38.
References. (1) ATLAS^{3D}, (2) MUSE (both excluding the data within the inner 1 arcsec radius circle).

measured in the diffuse gas of NGC 4469 is [OIII]λ5007 Å/Hβ = 1.19 ± 0.38.

Further evidence of the presence of a young stellar population in the ionised gas discs of the galaxies NGC 4429 and NGC 4476 comes from the imaging data in the FUV band gathered with the UVIT instrument on board the ASTROSAT space telescope (see Figs. 3 and 4). These images show a bright

structured and clumpy emission superimposed on a diffuse low surface brightness and extended emission, the former coming from recently formed HII regions associated with the ionised gas disc, the latter from the diffuse distribution of evolved stars in the thick and extended bulge of these lenticular galaxies (UV upturn; O'Connell 1999; Boselli et al. 2005). The same structured and clumpy emission of resolved HII regions is also observable in the VESTIGE images of NGC 4429, NGC 4459, NGC 4476, NGC 4477, and NGC 4526 (Fig. 1), or in absorption because of the presence of dust in the high-resolution HST images (Fig. 6). In the remaining galaxies NGC 4262 and NGC 4552, the filamentary structure of the ionised gas is similar to that observed in cooling flows. We remark, however, that some clumpy regions of ionised gas lie on the western side of NGC 4262, the brightest of which is located at RA(J2000) = 12h19m26ṣ6, Dec(J2000) = 14°52′30″with counterparts in the FUV ASTROSAT/UVIT image. These regions are also visible in the ring-like structure discovered by Bettoni et al. (2010) in the GALEX FUV image, and they are certainly associated with star-forming regions. NGC 4262 also has a two-arm spiral structure in the ionised gas close to the nucleus (see Figs. 1 and 2), again suggesting a rotating star-forming disc of ionised gas. In NGC 4469, the HII regions cannot be resolved because of the edge-on orientation of the disc. The disc, however, is very thin (≃100 pc) and clumpy, as expected if it is composed of star-forming regions.

4.3. Star formation activity

VESTIGE Hα+[NII] fluxes can be converted into star formation rates after they are corrected for dust attenuation and [NII] contamination. This can easily be done using the MUSE data in NGC 4469 and NGC 4526. Unfortunately, for the other VESTIGE sources, accurate IFU spectroscopic data such as those provided by MUSE are not available. Given their massive nature (see Table 1), we expect that all these galaxies are metal-rich objects with characteristics similar to those encountered in NGC 4469 and NGC 4526, where [NII]/Hα = 0.78 (derived excluding the nucleus of NGC 4526 because of a possible contamination of a nuclear activity, see Fig. 12). Similar values are also observed in the discs of NGC 4429 ([NII]/Hα ≃ 1.27) and NGC 4476 ([NII]/Hα ≃ 0.67) using the SOAR data. All these numbers are consistent with what is observed in star-forming objects of similar mass (Boselli et al. 2009). For the galaxies without any available spectroscopic data, we thus assume [NII]/Hα = 0.78.

Hα fluxes can be corrected for dust attenuation using two different methods. The first method uses the Balmer decrement, and the second uses the recipe of Calzetti et al. (2010) based on the 24μm *Spitzer*/MIPS data (see Boselli et al. 2015 for a comparison of the two methods).

4.3.1. A(Hα) from the Balmer decrement

An accurate estimate of the Balmer decrement is available only for NGC 4469 and NGC 4526 thanks to the MUSE data. In NGC 4429 and NGC 4476, the Balmer decrement is highly uncertain because of the weak Hβ emission. However, given their very similar spectroscopic properties, we assumed for these two objects the mean Balmer decrement measured within the discs of NGC 4469 and NGC 4526 (Hα/Hβ ≃ 5). For the remaining galaxies, we estimated the mean Balmer decrement from the 2D dust distribution derived using the broad-band NGVS images, as described in Sect. 4.4. The comparison between the 2D distribution of the dust attenuation derived using the Balmer decrement and that estimated after subtracting a model light distribution to the g-band image of NGC 4526 shows a fairly good agreement, with

$$A(\mathrm{H}\alpha) = 3.01 \times A(g), \quad (1)$$

corresponding to

$$E(B-V)_{BD} = 4.87 \times E(B-V)_{\mathrm{star}}, \quad (2)$$

where $E(B-V)_{BD}$ is the attenuation of the gaseous component as derived from the Balmer decrement, and $E(B-V)_{\mathrm{star}}$ is that of the stellar component derived from the g-band image. This exercise can be made only in this galaxy because the g-band image of NGC 4469 is saturated in the centre and has a pronounced boxy shape (Mosenkov et al. 2020) that can hardly be reproduced with a 2D fitting model. It therefore affects the determination of $A(g)$ in the star-forming disc and in the outer low surface brightness regions. The derived relation is steeper than the Calzetti law ($E(B-V)_{BD} = 2.27 \times E(B-V)_{\mathrm{star}}$; Calzetti et al. 2000), as expected for a screen dust distribution for the gaseous component and a slab distribution for the stellar component. An accurate estimate of $A(g)$ is possible for galaxies NGC 4459 and 4477. Assuming that the properties of their dust discs are comparable to the disc observed in NGC 4526, we used their mean values of $A(g)$ derived within the disc combined with Eq. (1) to estimate A(Hα) and to correct the observed Hα fluxes for dust attenuation. This value is derived on the disc region where dust is seen in absorption, which for geometrical effects fairly corresponds to half of the disc. The value was then extrapolated to the rest of the disc.

4.3.2. A(Hα) from the 24 μm *Spitzer*/MIPS emission

The dust attenuation correction based on the 24 μm *Spitzer*/MIPS emission assumes that the energy of the ionising radiation absorbed by dust is re-radiated in the mid-infrared. This correction is given by the relation (Calzetti et al. 2010)

$$L(\mathrm{H}\alpha)_{\mathrm{Cor}} = L(\mathrm{H}\alpha)_{\mathrm{Obs}} + 0.020 \times L(24\,\mu\mathrm{m}), \quad (3)$$

which is valid for $L(24\,\mu\mathrm{m}) \leq 4 \times 10^{42}$ erg s^{-1}, the range covered by the S0 galaxies analysed in this work. For this purpose, we have derived the 24 μm flux densities of the eight target galaxies using the photometric extraction presented in Fossati et al. (2018) optimised to integrate within a given aperture and estimate a statistically robust uncertainty. This procedure was run on the homogeneously reduced dataset of Bendo et al. (2012a).

The Hα luminosities derived using the two independent methods are fairly consistent, as indicated in Fig. 13. The dispersion in the relation is comparable to that observed in the calibration of Calzetti et al. (2007, 2010) (~0.3 dex) or in the same relation observed in normal late-type galaxies (Boselli et al. 2015). Part of the scatter, however, can come from the large uncertainty on the derived Balmer decrement from the optical dust attenuation maps.

4.3.3. Conversion of Hα luminosities into SFR

The Hα luminosities of the target galaxies can be converted into star formation rates (SFR in units of $M_{\odot}$ yr^{-1}) assuming that the ionising radiation comes from young stars that formed at a constant rate over ≳10 Myr in the disc of ionised gas (e.g. Kennicutt 1998a; Boselli et al. 2009). This assumption is reasonable for galaxies in which the emission comes from clearly

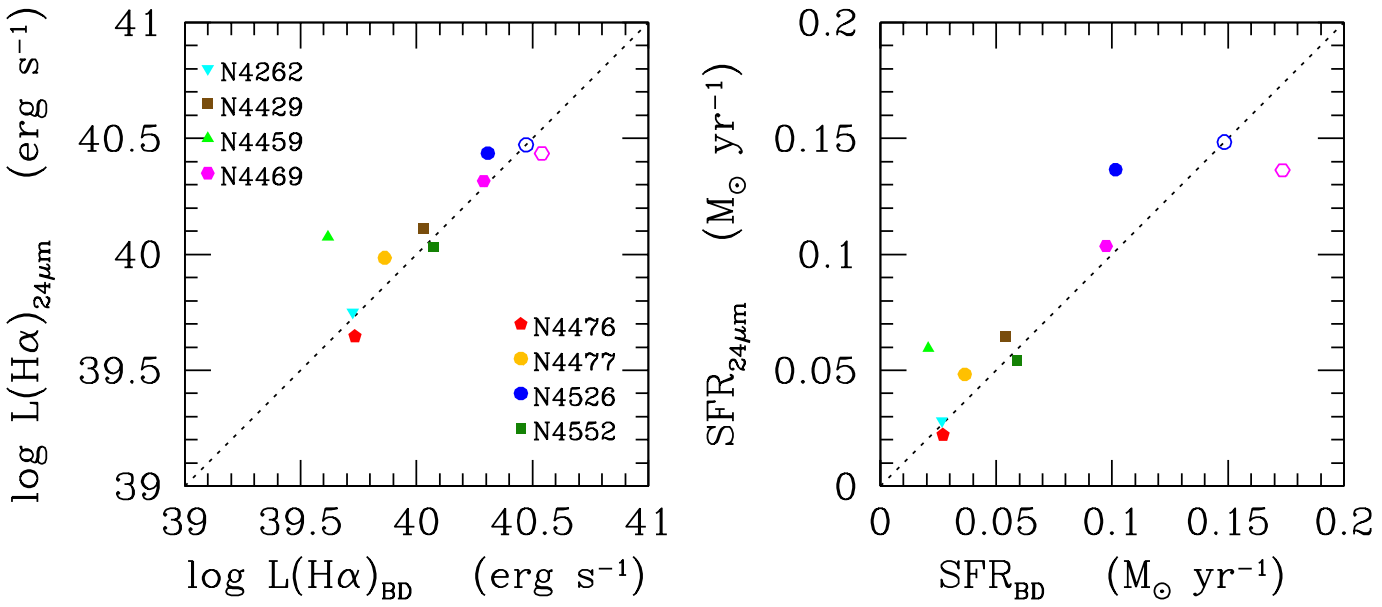

Fig. 13. *Left*: comparison between the Hα luminosity corrected for dust attenuation derived using the 24μm *Spitzer*/MIPS emission ($L(\mathrm{H}\alpha)_{24\mu m}$) and that derived using the Balmer decrement ($L(\mathrm{H}\alpha)_{BD}$), as described in the text. Both luminosities are corrected for [NII] contamination. Different symbols indicate different galaxies. Filled symbols are for Hα narrow-band data, and open symbols represent MUSE data. The dotted line shows the one-to-one relation. *Right*: same comparison for the star formation rates derived using the Kennicutt (1998a) calibration adapted for a Chabrier (2003) IMF.

delimited discs (NGC 4429, 4459, 4469, 4476, 4477, and 4526), while it might be unrealistic for the remaining two galaxies (NGC 4262 and 4552), in which the Hα emission partly comes from diffuse filaments. Assuming the Kennicutt (1998a) calibration, a Chabrier (2003) initial mass function (IMF), and a mean value for the attenuation as estimated above, the total star formation rates of these galaxies are $0.02 \lesssim \mathrm{SFR} \lesssim 0.15 M_\odot\,\mathrm{yr}^{-1}$ (see Table 1). Their star formation activity is more than a factor of ten lower than that of late-type galaxies of similar stellar mass, which positions them well below the main sequence (Boselli et al. 2015; see Fig. 14). Because the discs are small ($0.7 \lesssim R(\mathrm{H}\alpha) \lesssim 2.0$ kpc), however, their typical star formation surface density is $0.004 \lesssim \Sigma(\mathrm{SFR}) \lesssim 0.02\,M_\odot\,\mathrm{yr}^{-1}\,\mathrm{kpc}^{-2}$. This is comparable to that of larger discs that characterise gas-rich spiral galaxies (Kennicutt 1998b; Bigiel et al. 2008).

4.3.4. Physical properties of individual HII regions

Using the same procedures as were adopted in Boselli et al. (2020, 2021b) based on the HIIPHOT data reduction pipeline (Thilker et al. 2000), we identified the HII regions and derived their properties in the discs of galaxies NGC 4429, 4459, 4476, 4477, and 4526. We refer to these papers for an accurate description of the code and of its use on the VESTIGE NB imaging data. We excluded galaxies NGC 4262 and NGC 4552 because of their filamentary ionised gas emission, which is not unambiguously associated with any well-identified star-forming complex, and NGC 4469 because it is an edge-on system in which individual HII regions cannot be resolved for projection effects. Because the stellar continuum in the inner regions of these lenticular galaxies is bright, we limited this analysis to the HII regions with $L(\mathrm{H}\alpha) \geq 10^{37}\,\mathrm{erg\,s}^{-1}$ and equivalent radii $r_{\mathrm{eq}}(\mathrm{H}\alpha) \gtrsim 50$ pc, which are defined as the radii of the circles of surface equivalent to the area of the detected HII region down to a surface brightness limit of $\Sigma(\mathrm{H}\alpha) = 3 \times 10^{-17}\,\mathrm{erg\,s}^{-1}\,\mathrm{cm}^{-2}$ (Helmboldt et al. 2005). As in Boselli et al. (2021b), equivalent radii and diameters were corrected for the effects of the point-spread function. This analysis is intended to trace the statistical properties of the HII regions in the discs of these lenticular galaxies. HIIPHOT detects 42, 61, 14, 28, and 48 HII regions satisfying these criteria in the galaxies NGC 4429, 4459, 4476, 4477, and 4526, respectively.

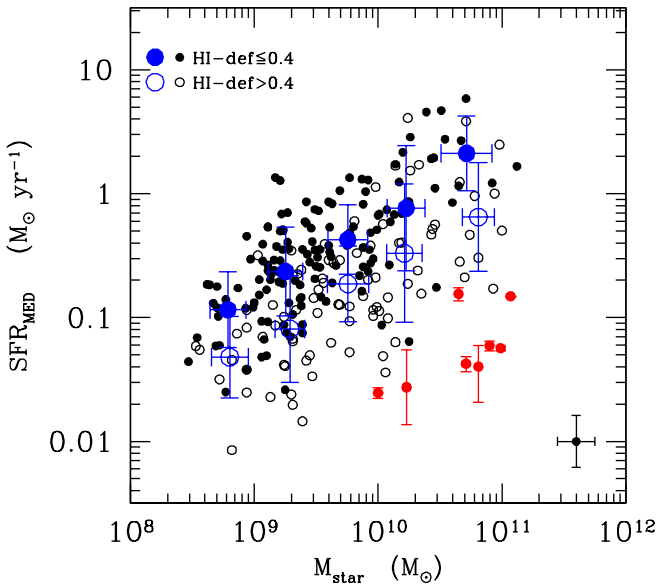

Fig. 14. Relation between the star formation rate and the stellar mass for the *Herschel* Reference Survey (HRS) late-type galaxies, adapted from Boselli et al. (2015). Filled black dots are for HI-normal (HI − def $\leq$ 0.4) field galaxies, and empty black circles show HI-deficient (HI − def > 0.4) cluster objects. The large filled and empty blue circles give the mean values and the standard deviations in different bins of stellar mass. The black error bar in the lower right corner shows the typical uncertainty on the data. The lenticular galaxies analysed in this work are indicated by the filled red dots.

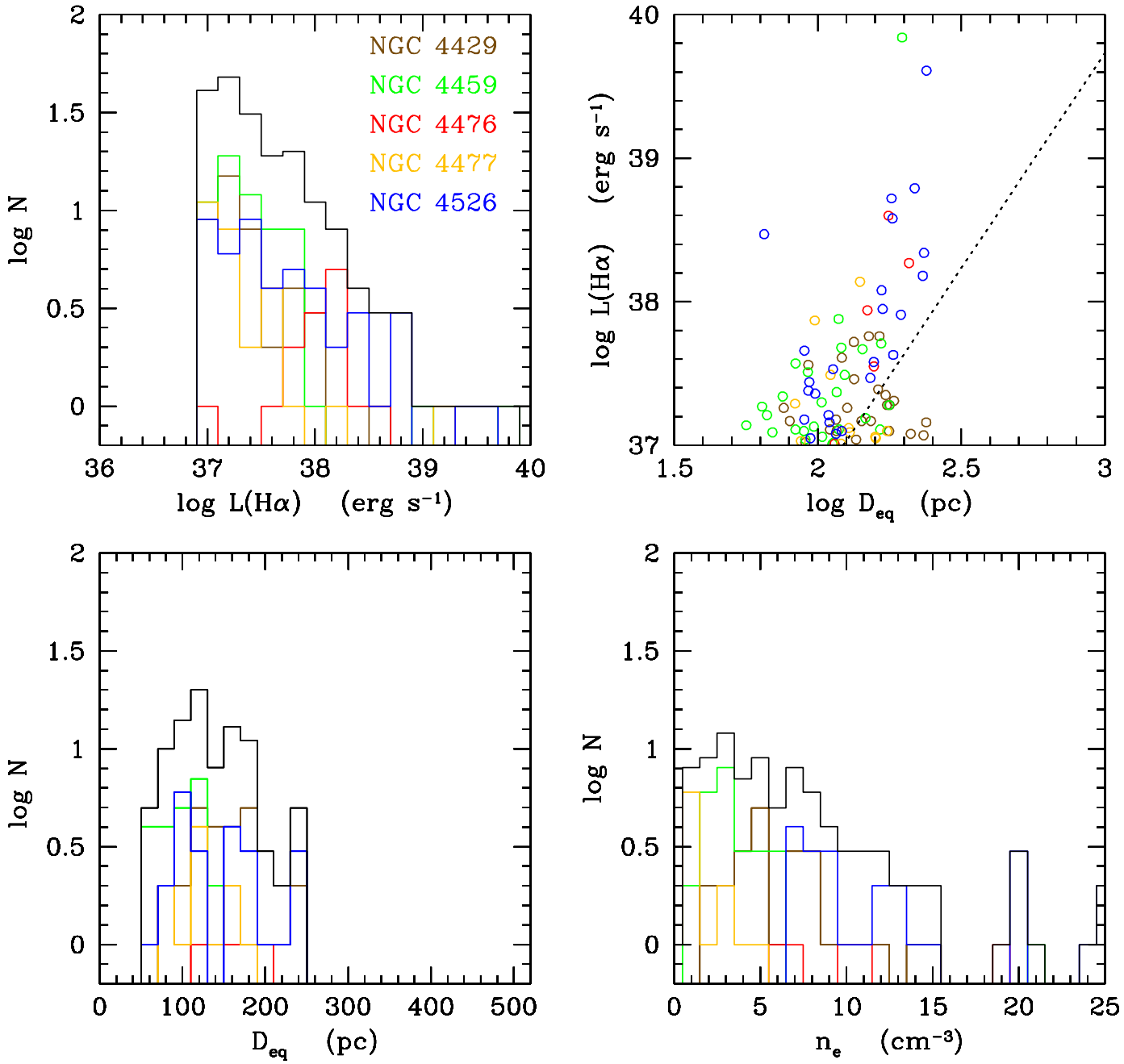

Fig. 15. Statistical properties of the HII regions of the S0 galaxies with luminosity $L(\mathrm{H}\alpha) \geq 10^{37}$ erg s^{-1} and $S/N > 5$. *Upper left*: Hα luminosity function. *Upper right*: relation between the Hα luminosity and the equivalent diameter. *Lower left*: distribution of the equivalent diameter. *Lower right*: distribution of the electron density. Galaxies are colour-coded as follows: Brown for NGC 4429, green for NGC 4459, red for NGC 4476, orange for NGC 4477, and blue for NGC 4526. The black histogram gives the cumulative distribution for all objects. All the Hα luminosities are corrected for [NII] contamination assuming [NII]/Hα = 0.78. Electron densities are also corrected for dust attenuation for comparison with other studies.

Figure 15 shows the principal statistical properties of the HII regions in the discs of the five lenticular galaxies. All the Hα fluxes were corrected for [NII] contamination assuming [NII]/Hα = 0.78 as measured on the disc of NGC 4469 and 4526 using the MUSE data. For comparison with other works, Hα luminosities were not corrected for dust attenuation, except for the electron density n_e, where Hα luminosities were estimated using the same $A(\mathrm{H}\alpha)$ as derived in Sect. 4.3.1 ($A(\mathrm{H}\alpha)$ = 1.433, 0.418, 1.433, 0.186, and 1.543 mag for NGC 4429, 4459, 4476, 4477, and 4526, respectively). Compared to those observed in the ram pressure perturbed dwarf galaxy IC 3476 (Boselli et al. 2021b), the HII regions in the discs of these lenticular galaxies typically have a lower luminosity and a smaller size. The only galaxy with HII regions of luminosity $L(\mathrm{H}\alpha) > 10^{39}$ erg s^{-1} is NGC 4526 (two regions). Bright HII regions can be formed by the compression of the gas induced by a ram pressure stripping event during the first interaction of the galaxy ISM with the surrounding ICM (e.g. Boselli et al. 2021b). The phase-space diagram shown in Fig. 16 suggests that NGC 4526 is a first infaller, consistent with this interpretation. A complete and detailed comparative analysis with the physical properties of HII regions in a large sample of spiral galaxies spanning a wide range

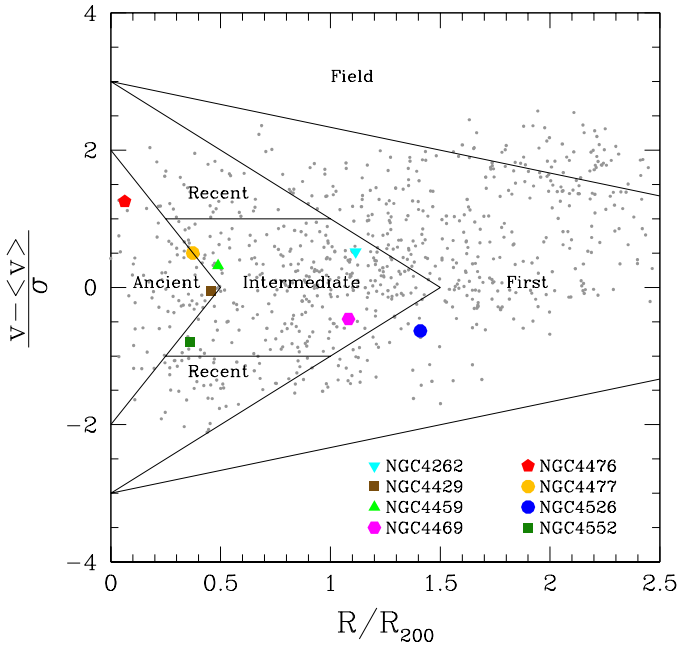

Fig. 16. Distribution of the eight lenticular galaxies within the phase-space diagram traced by galaxies within the Virgo cluster. Grey dots indicate the Virgo cluster galaxies with a recessional velocity <3500 km s^{-1} extracted from the sample of Boselli et al. (2014a). The solid lines delimit the different regions extracted from the simulations of Rhee et al. (2017) to identify galaxies in different phases of their infall into the cluster: First (not yet fallen), recent ($0 < \tau_{\rm inf} < 3.6$ Gyr), intermediate ($3.6 < \tau_{\rm inf} < 6.5$ Gyr), and ancient ($6.5 < \tau_{\rm inf} < 13.7$ Gyr) infallers.

in morphological type and stellar mass will be made when the VESTIGE survey is completed.

4.4. Dust content and distribution

The high-quality HST images (Fig. 6) and the NGVS/VESTIGE optical images (Fig. 5) show dust structures in absorption. Prominent dusty discs with a clear spiral structure are present in the HST images of NGC 4429, 4459, 4476, and NGC 4526. A thin edge-on dusty disc with filaments extending in the z-direction is visible in NGC 4469. Thin and extended filaments spiraling around the nucleus of the galaxy are visible in NGC 4477 ($F475W$). A very smooth and limited filament of dust in absorption is also seen in the northern direction in NGC 4552 ($F555W$), while NGC 4262 does not have any clear dust structure.

For each object, we constructed a 2D model of the stellar distribution and subtracted it from the NGVS g-band optical images (Ferrarese et al. 2012). These images cover the whole extent of the galaxies and not only a fraction of them, as in the HST images, thus they can be used to derive the dust distribution seen in absorption, exactly as was done for M87 in Boselli et al. (2019), or for other lenticular galaxies with ionised gas emission and prominent dust features (e.g. Patil et al. 2007; Finkelman et al. 2010; Kulkarni et al. 2014). For this exercise, we integrated the model-subtracted image within a region positioned over the disc of dust as seen in absorption (see Fig. 17). We then transformed the attenuation map $A(g)$ first in $A(V)$ with a Milky Way extinction curve, then in $\Sigma_{\rm dust}$ using the relation (Spitzer 1978; Kitayama et al. 2009)

Table 8. Dust masses.

NGC	$M_{\rm dust}$(SED)	$M_{\rm dust}(A(g))$	G/D [b]
Units	$M_\odot$	$M_\odot$	
4262	–	–	–
4429	$1.83\times10^6\pm2.9\times10^5$	5.0×10^4	86.1 (226.4)
4459	$1.50\times10^6\pm1.1\times10^5$	2.4×10^4	90.5 (318.4)
4469 [a]	$7.67\times10^6\pm3.8\times10^5$	2.0×10^4	–
4476	$1.06\times10^6\pm1.4\times10^5$	5.7×10^3	67.1 (138.1)
4477	$5.81\times10^5\pm1.3\times10^5$	4.0×10^4	30.9
4526	$9.95\times10^6\pm1.6\times10^6$	9.4×10^4	40.8 (31.6)
4552	$6.02\times10^6\pm3.8\times10^6$	–	–

Notes. [a]$A(g)$ measured only within the star-forming disc, thus the dust mass coming from $A(g)$ is a lower limit because filaments of dust are seen outside the selected region. [b]Gas-to-dust ratio measured using dust masses derived from the SED fitting analysis and molecular gas masses with CARMA (and ALMA) data.

$$A(V) = 0.011\left(\frac{Q_{\rm ext}}{2}\right)\left(\frac{\Sigma_{\rm dust}}{10^3 M_\odot\ {\rm kpc}^{-2}}\right)\left(\frac{\rho_{\rm dust}}{3{\rm g\ cm}^{-3}}\right)^{-1}\left(\frac{a}{0.1\,\mu{\rm m}}\right)^{-1}, \quad (4)$$

where $Q_{\rm ext}$ is the extinction coefficient factor, $\rho_{\rm dust}$ is the dust mass density, and a is the grain radius, adopting the standard values given in the equation. The total dust mass was then derived assuming that the dust is uniformly distributed over the disc associated with the ionised gas. The extinction maps give dust masses of about $6\times10^3 \lesssim M_{\rm dust} \lesssim 9\times10^4\ M_\odot$.

To determine the reliability of this method, we compared the total dust masses derived in this way with those calculated by fitting the observed spectral energy distribution of each galaxy with the CIGALE spectral energy distribution (SED) fitting code (Noll et al. 2009; Boquien et al. 2019; see Table 8). Because the dusty disc is located only within the very inner regions compared to the much more extended stellar emission, we determined the total dust mass by fitting only the spectral bands in which the emission is dominated by dust, including WISE at 22 μm, *Spitzer*/MIPS at 24 and 70 μm, and *Herschel* Photodetector Array Camera and Spectrometer (PACS) and Spectral and Photometric Imaging Reciver (SPIRE) at 100, 160, 250, 350, and 500 μm (8 bands in total). The emission of early-type galaxies in the mid-IR might be contaminated by that of stellar envelopes (Boselli et al. 1998; Temi et al. 2009; Ciesla et al. 2014). We thus first removed the contribution from the stellar emission to the WISE 22 μm and *Spitzer*/MIPS 24 μm bands as in Ciesla et al. (2014). We estimated this contamination by fitting the stellar SED (from the FUV to the K band, in ten photometric bands) of each galaxy again with CIGALE. For this purpose, we used Bruzual & Charlot (2003) stellar population models, a Chabrier (2003) IMF, and a delayed star formation history such as described in Boquien et al. (2019). We then fit the infrared SED using the Draine & Li (2007) dust models, consistently with Ciesla et al. (2014) and Boselli et al. (2016b). The dust masses of these galaxies are $6\times10^5 \lesssim M_{\rm dust} \lesssim 10^7\ M_\odot$ (see Table 8), which is a factor of ≃50 lower than those of star-forming systems of similar stellar mass (Cortese et al. 2012).

These dust masses are a factor of 14–380 higher than those derived from dust absorption. These differences are too large to be ascribed to the uncertainties in the determination of the dust attenuation map or to the determination of the dust distribution

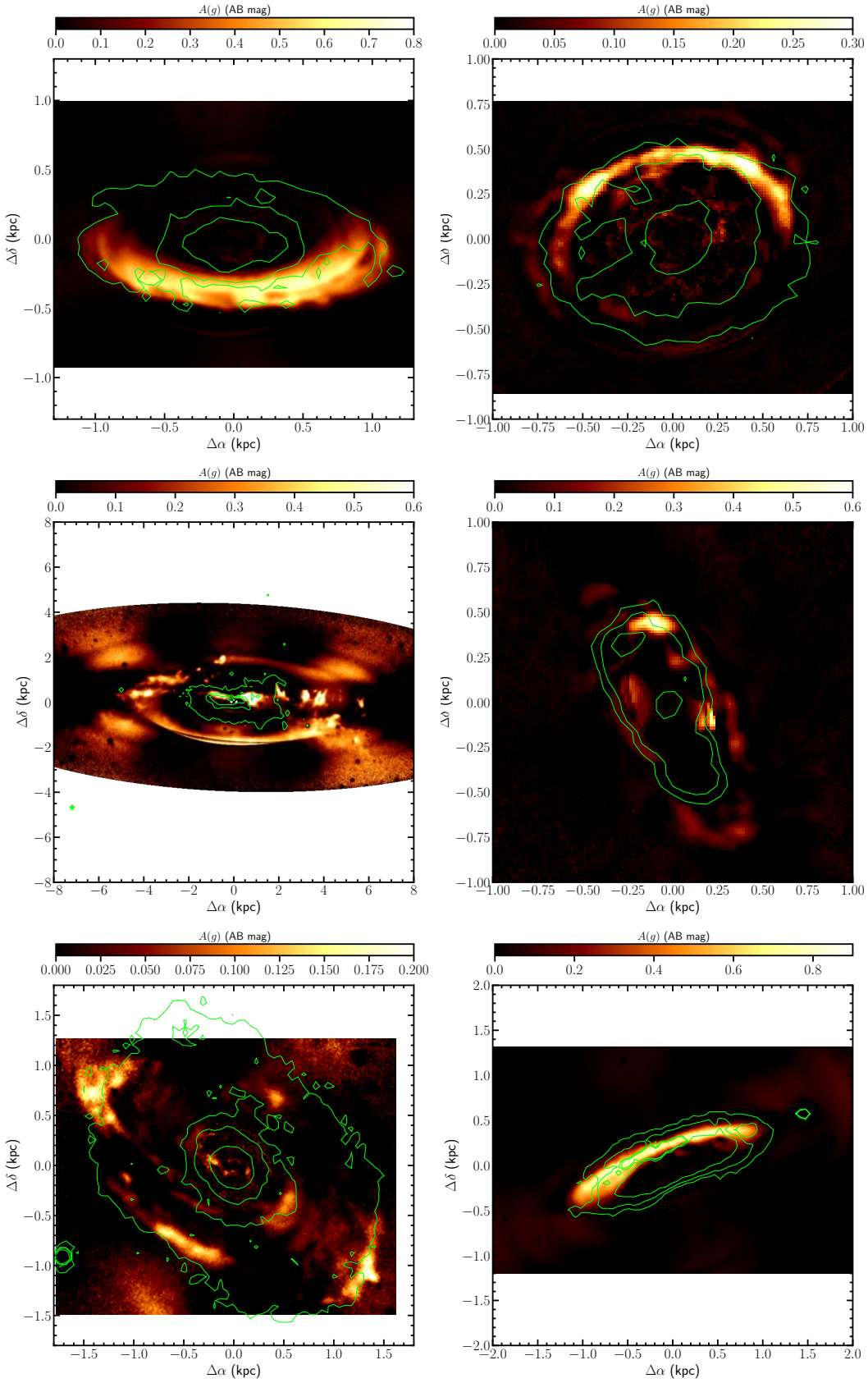

Fig. 17. $A(g)$ extinction maps of the galaxies NGC 4429 (*first row, left*), 4459 (*first row, right*), 4469 (*second row, left*), 4476 (*second row, right*), 4477 (*last row, left*), and 4526 (*last row, right*), with contour levels of the VESTIGE Hα emission. Contours are at 3×10^{-16}, 6×10^{-16}, 1.5×10^{-15} erg s^{-1} cm^{-2} arcsec^{-2} for galaxies NGC 4429, 4459, 4476, and 4526, and at 10^{-16}, 3×10^{-16}, 6×10^{-16}, 1.5×10^{-15} erg s^{-1} cm^{-2} arcsec^{-2} for galaxies NGC 4469 and 4477. The colour scale of the $A(g)$ extinction maps of galaxy NGC 4469 reaches negative values to take into account the low-frequency gradients that are not removed by the fitted model and relative to the prominent boxy shape of the bulge.

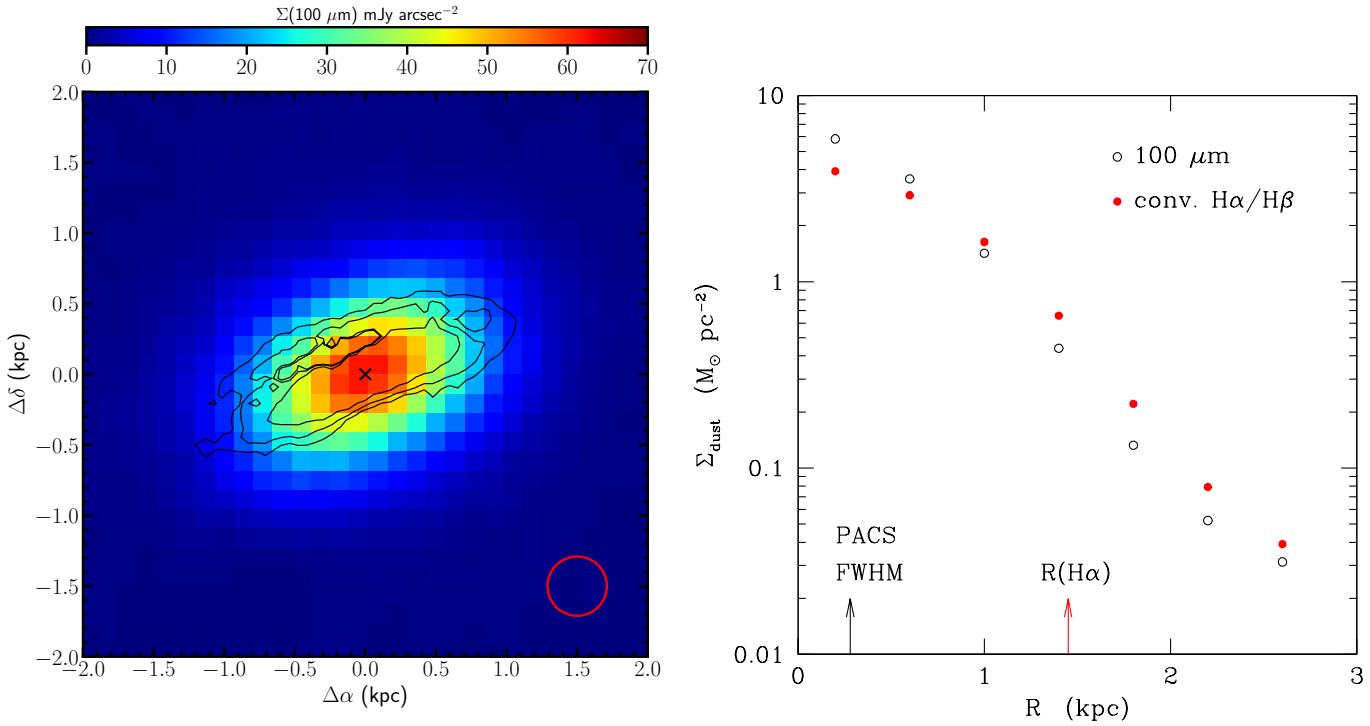

Fig. 18. *Left*: *Herschel*/PACS image of galaxy NGC 4526 at 100 μm (from Cortese et al. 2014), in units of mJy arcsec^{-2}, with contour levels of the VESTIGE Hα emission (3×10^{-16}, 6×10^{-16}, 1.5×10^{-15} erg s^{-1} cm^{-2} arcsec^{-2}). The black cross indicates the position of the galaxy centre. The red circle in the lower right corner gives the FWHM of the PACS data (7″). *Right*: radial variation of the dust surface density profile of NGC 4526 derived from the PACS 100 μm image (empty black circles) and from the $E(B-V)$ 2D map derived using the Balmer decrement extracted from the MUSE data cube and brought to the same resolution as PACS, as described in the text (filled red circles). The vertical black and red arrows indicate the PACS FWHM and the extension of the Hα emitting disc.

within the disc. As already widely discussed in the literature, this discrepancy might have two different origins. We list them below.

First, as remarked by Goudfrooij & de Jong (1995) for the first time, dust masses derived from optical dust absorption maps should be taken as lower limits because Eq. (4) is valid in a screen model, that is, when the emitting stars are all located behind the dust. This is obviously not the case in lenticular galaxies, in which the dust disc lies within the plane of the galaxy (sandwich model). This means that about half of the stars of the prominent bulge are located in between the dust and the observer.

Second, dust masses derived using SED fitting techniques might include a diffuse and unstructured dust component. If present, this component would be subtracted along with the stellar component from the optical images since included in the fitted model. The excess of dust mass derived from SED fitting might thus indicate the presence of diffuse dust produced, injected into the ISM (Goudfrooij & de Jong 1995; Dwek 1998; Zhukovska et al. 2008; Valiante et al. 2009; Triani et al. 2020), and heated by the old stellar population that is dominant in early-type systems (Boselli et al. 2010b, 2012; Bendo et al. 2012b, 2015).

To determine whether the extended emission observed in the PACS bands is due to a diffuse dust component or to the component that is associated with the ionised gas disc, we convolved the $E(B-V)_{BD}$ 2D map of NGC 4526 derived using the Balmer decrement extracted from the MUSE data with the 100 μm PACS PSF given in Bocchio et al. (2016) for fast-scan observations in parallel mode (Cortese et al. 2014). We then extracted the radial profile of the 100 μm PACS emission and of the convolved $E(B-V)_{BD}$ 2D map in concentric elliptical annuli centred on the nucleus of the galaxy with a size increasing by 0.4 kpc. We then converted the measured 100 μm surface brightnesses into dust surface densities using the relation (e.g. Spitzer 1978; Boselli 2011)

$$M_{\rm dust} = \frac{S(\nu)D^2}{K_\nu B(\nu,T)}, \tag{5}$$

where $S(\nu)$ is the PACS flux density at 100 μm and D is the distance of the galaxy. We then assumed a dust grain opacity at 100 μm $K_{100} = 27.15\,{\rm cm^2\,g^{-1}}$ (Draine 2003) and a dust temperature $T = 22.6$ K, at which temperature the total dust mass estimated from the CIGALE SED fitting analysis ($M_{\rm dust} = 9.95\times10^6\,M_\odot$) becomes equal to the mass given in Eq. (5) after it is integrated over all the increasing elliptical annuli. We then compared this dust radial profile derived from the 100 μm PACS data to the profile derived from the convolved MUSE Balmer decrement in Fig. 18, where $E(B-V)_{BD}$ is converted into $\Sigma_{\rm dust}$ using Eq. (4) and normalised to the total dust content of the galaxy, as for the PACS profile. The radial variations in the two profiles are very similar, clearly indicating that the extended 100 μm emission of NGC 4526 is due to the dust that is frozen into the circumnuclear ionised gas disc. Because NGC 4526 is the galaxy of the sample with the most extended 100 μm emission with respect to that of the diffuse ionised gas, we argue that this conclusion is probably also valid for the other objects.

In agreement with the results obtained in other studies based on the analysis made using 3D radiative transfer models of early-type galaxies with similar dust features (Viaene et al. 2015, 2019), we conclude that in these lenticular galaxies, the observed difference between the dust content estimated from optical absorption features and from the SED fitting analysis

is mainly due to geometrical effects related to the relative distribution of the absorbing dust and the emitting stars. We note that the importance of geometry is corroborated by two other results mentioned above: (a) The dust features seen in absorption in the HST images (Fig. 6) and in the $A(g)$ attenuation maps (Fig. 17) are asymmetric and strongly depend on the orientation of the galaxy discs with respect to the line of sight. (b) In NGC 4526, where the data allowed a direct comparison, $E(B-V)_{BD} = 4.87 \times E(B-V)_{\rm star}$, thus significantly flatter than the canonical Calzetti law observed in starburst galaxies (Calzetti et al. 2000, see Sect. 4.3.1), where the dust layer thickness is comparable to that of the stellar disc (slab model). Furthermore, $E(B-V)_{BD}$ is fairly symmetric because the young and massive stars that cause the ionising radiation and the absorbing dust are well mixed within the disc as in a slab model, while this is not the case for the dominant old stellar population, which is distributed in a much thicker and extended lenticular bulge (sandwich model).

4.5. Cold-gas content

Interferometric data in the CO lines can be used to derive the molecular gas content and distribution within the target galaxies. Five galaxies (NGC 4429, 4459, 4476, 4477, and 4526) have been observed with CARMA in the ^{12}CO(1–0) line with a typical angular resolution of $3'' \lesssim FWHM \lesssim 9''$ at a sensitivity that is sufficient to detect molecular gas in diffuse and extended structures. Assuming a constant CO-to-H_2 conversion factor $X_{\rm CO} = 2.3 \times 10^{20}$ cm^{-2}/(K km s^{-1}) (Strong et al. 1988), which is appropriate for massive galaxies such as these (e.g. Boselli et al. 2002; Bolatto et al. 2013), we derived the molecular gas masses given in Table 5. These molecular gas masses can be compared to those derived using different sets of ALMA data, which have the advantage of being at a much higher angular resolution than the CARMA data. ALMA data for two galaxies are in the ^{12}CO(2–1) line and for one in the ^{12}CO(3–2) line. Using the same procedure as applied to the CARMA data, and assuming the ratios ^{12}CO(2–1)/^{12}CO(1–0) = $0.65^{0.83}_{0.50}$ and ^{12}CO(3–2)/^{12}CO(1–0) = $0.31^{0.42}_{0.20}$ from Leroy et al. (2021), which is quite consistent with previous values (e.g. Leroy et al. 2009; Wilson et al. 2012), we estimated total molecular hydrogen masses from the ALMA data. The two sets of data are fairly consistent (see Table 5). The values given in Table 1 are, in order of priority, the 12 m ALMA or CARMA data, whenever two sets of data are available, with a typical uncertainty of ∼0.1 and 0.2 dex, respectively, estimated from the comparison of the 12 m and 7 m ALMA data, or the comparison of the ALMA and CARMA data. We recall that the ALMA data might include an additional systematic uncertainty due to the poorly constrained ^{12}CO(2–1)/^{12}CO(1–0) and ^{12}CO(3–2)/^{12}CO(1–0) ratios, which, because of the peculiar physical properties of the gas discs analysed in this work, might be different than those assumed here and derived from the observation of normal star-forming galaxies (e.g. Hafok & Stutzki 2003). For galaxies NGC 4469 and NGC 4552, molecular gas masses were derived as indicated in the next session.

4.6. Gas-to-dust ratio

The same set of data can be used to estimate the typical gas-to-dust ratio of these lenticular galaxies and compare it to that of late-type galaxies with similar metallicity. It has been shown that in the Milky Way, in the nearby Magellanic clouds, or in other nearby galaxies, where the angular distribution of the data allows us to trace the ratio of the gas-to-dust column density in different environments, $\Sigma_{\rm gas}/\Sigma_{\rm dust}$ varies only as a function of the metallicity (e.g. Dwek 1998; Issa et al. 1990; Sandstrom et al. 2013; Roman-Duval et al. 2014; Mattsson & Andersen 2012; Mattsson et al. 2014; Giannetti et al. 2017). Because all the analysed objects are massive and thus probably metal rich, if the gas and dust have an internal origin, we expect a constant gas-to-dust ratio close to the ratio that is measured in the solar neighbourhood ($\Sigma_{\rm gas}/\Sigma_{\rm dust}(Z_\odot)$ = 100–160, Sodroski et al. 1994; Draine et al. 2007), where the oxygen abundance is 12+log O/H($Z_\odot$) = 8.69 (Asplund et al. 2009). Because we measure dust and gas masses rather than column densities, we have to assume that the different phases of the ISM have a similar distribution, as observations indeed indicate (see Fig. 6). The total gas mass can be derived by combining the molecular and the atomic components. Of the eight galaxies, only three have been detected in HI (NGC 4262; Serra et al. 2012; NGC 4469 and NGC 4526; Haynes et al. 2018). For all the others, the measured upper limits to their HI mass are significantly lower than the measured molecular gas masses. We can thus confidently assume that the total gas is dominated by the molecular gas phase. This is consistent with the observed physical association between the dust distribution and the molecular gas distribution, which is stronger than that with the atomic gas phase whenever the molecular gas is the dominant phase (Dame et al. 2001; Sandstrom et al. 2013). We recall that galaxies NGC 4459, NGC 4477, NGC 4526, and NGC 4552 have hot-gas masses of $4 \times 10^7 \lesssim M_{\rm hot} \lesssim 2.3 \times 10^8\ M_\odot$ (Su et al. 2015), which is comparable to the molecular gas masses. Because it is diffuse and generally not associated with the dust component, this hot-gas phase is not accounted for in the estimate of the gas-to-dust ratio.

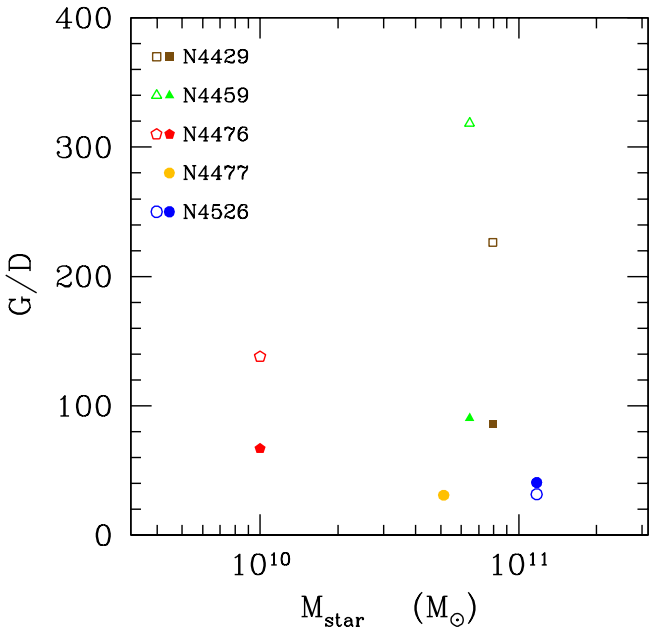

Fig. 19. Relation between the volumetric gas-to-dust (G/D) ratio of the target galaxies measured using the CARMA (filled symbols) and ALMA (empty symbols) data and their stellar mass. Different symbols indicate different galaxies.

Figure 19 shows the relation between the volumetric gas-to-dust (G/D) ratio of the target galaxies (see Table 8) and their stellar mass, with dust masses derived from the SED fitting analysis. Figure 19 indicates that the gas-to-dust ratio of these lenticular galaxies ranges between $30 \lesssim G/D \lesssim 320$,

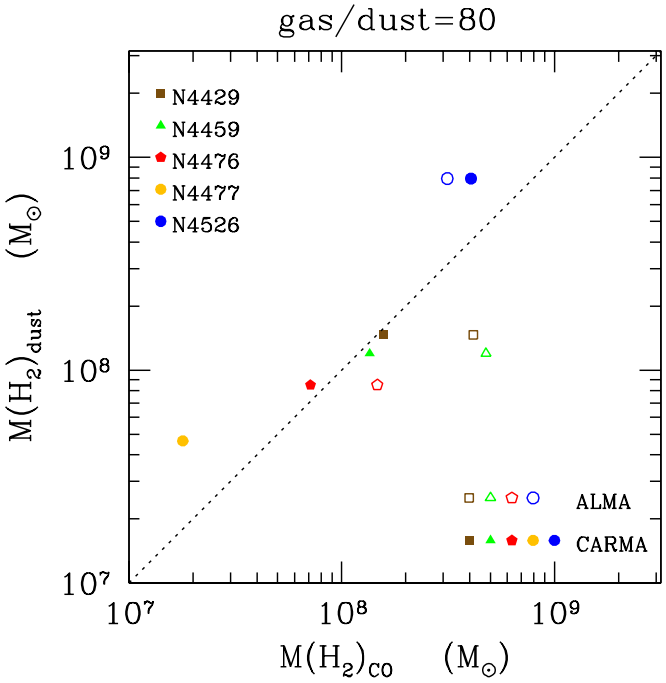

Fig. 20. Relation between the molecular gas mass derived using the total dust mass and assuming a gas-to-dust ratio of $G/D = 80$ and the molecular gas mass derived using CO observations for galaxies with ALMA (empty symbols) and CARMA (filled symbols) data. The different galaxies are indicated by different symbols. The dotted line shows the expected relation for a gas-to-dust ratio $G/D = 80$.

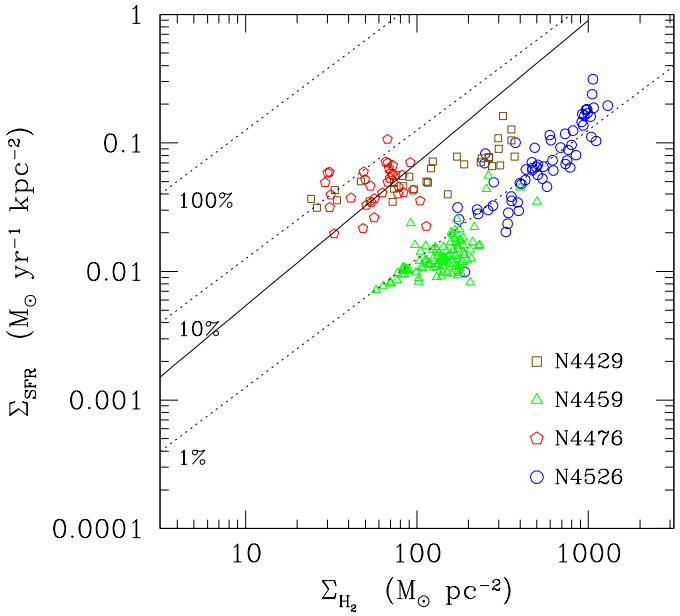

Fig. 21. Relation between the star formation rate surface density and the molecular gas surface density at scales of ≃100 pc. Different symbols indicate different galaxies. The solid black line shows the best fit obtained by Bigiel et al. (2008) (scaled to the same X_{CO} conversion factor) for the Heracles sample of nearby galaxies using star formation rates derived from Hα+24μm flux surface densities. The dotted lines show lines of constant star formation efficiency, indicating the level of Σ_{SFR} needed to consume 1%, 10%, and 100% of the gas reservoir (including helium) in 10^8 years, corresponding to depletion times of 10^8, 10^9, and 10^{10} years.

and thus corresponds to the low range of the envelope sampled by similar massive late-type systems ($20 \lesssim G/D \lesssim 1000$) by Rémy-Ruyer et al. (2014). A value of $G/D \simeq 80$ is very consistent with the oxygen abundance of the gas in NGC 4469 and NGC 4526 (12+log O/H ≃ 8.75–8.80) as derived with the MUSE data, which is slightly higher than solar. The only exception is NGC 4262, which has a large amount of HI gas ($5.6 \times 10^8\ M_\odot$) and is undetected in CO (Boselli et al. 2014b) and in the far-IR (Ciesla et al. 2012; Cortese et al. 2014). The large amount of HI gas suggests that in this galaxy, the different phases of the ISM might not be distributed within the same region. The HI map of NGC 4262 indeed reveals that the atomic gas is mainly located in a disc that is much more extended than the stars (≃30 kpc in diameter; Serra et al. 2012). It is thus conceivable that part of this HI, the part that is located far from the core of the galaxy, is metal poor and thus poor in dust and molecular gas. Furthermore, this gas has a very low column density that is not sufficient to cause it to collapse into giant molecular clouds. This analysis indicates that we can obtain a rough estimate of the molecular gas mass of galaxies NGC 4469 and NGC 4552 from their total dust masses assuming a typical gas-to-dust ratio of $G/D = 80$, as depicted in Fig. 20, where the molecular gas masses derived using a constant gas-to-dust ratio and those measured using CO data are compared. These values are given in Table 1 with a typical uncertainty of 0.3 dex that roughly corresponds to the scatter in the relation shown in Fig. 20. The value derived for NGC 4552, $\log M(H_2) = 8.68 \pm 0.3\ M_\odot$, is slightly higher than the upper limit derived from CO observations in Boselli et al. (2014b), $\log M(H_2) < 8.37\ M_\odot$, but still within the assumed uncertainty.

4.7. Schmidt relation

The previously discussed data set allows us to trace the relation between the star formation rate surface density, Σ_{SFR}, and the molecular gas surface density, Σ_{gas}, generally called the Schmidt law (Schmidt 1959; Kennicutt 1998b), in five galaxies (NGC 4429, 4459, 4476, 4477, and 4526) at kiloparsec scales using the CARMA data, and in NGC 4429, NGC 4459, NGC 4476, and NGC 4526 at ∼100 pc scales using the ALMA data (Fig. 21). For this purpose, we convolved the ALMA moment-0 images of NGC 4429, NGC 4459, and NGC 4476 to the resolution of the Hα NB images (0.70″, 0.86″, and 0.86″, respectively), and the VESTIGE image of NGC 4526 to the resolution of the ALMA moment-0 image (1.14″ × 0.76″). We then rebinned the images to 1.2″pixels to have an independent signal in each corresponding position, and removed pixels with a low S/N ($S/N < 5$). We also removed the central ($\lesssim$2″) pixels, which might be contaminated by nuclear activity or by artifacts due to the continuum subtraction procedure, which is highly uncertain in these regions where the emission is very peaked and where saturated pixels might be present.

Figure 21 indicates that the star-forming discs of these four galaxies follow the Schmidt relation drawn by late-type galaxies, but with higher values of star formation ($0.01 \lesssim \Sigma_{SFR} \lesssim 0.3\ M_\odot\ yr^{-1}\ kpc^{-2}$) and molecular gas surface densities ($20 \lesssim \Sigma_{H_2} \lesssim 1000\ M_\odot\ pc^{-2}$). These values, which at a first glance might seem very high for these quiescent systems, can be explained considering that the inner discs are very dust rich, as indicated by their HST images (Fig. 6) and by the other multifrequency data presented above. Based on the tight relation between dust and gas column density, these discs also have very high molecular gas column densities. Figure 21 also shows, however,

that the molecular gas is transformed into stars with an efficiency ∼2.5 times lower than that measured in the discs of star-forming galaxies, but on a spatial scales that are significantly smaller (100 pc vs. 0.75 kpc, Bigiel et al. 2008). This is in line with the results of Davis et al. (2014) and Ellison et al. (2021). A similar result is obtained using the CARMA data at a much coarser angular resolution. The star formation efficiency observed in these S0 galaxies is, however, significantly higher than that observed in early-type objects that formed after a minor merging event (e.g. van de Voort et al. 2018). This result has been interpreted by Davis et al. (2014) as due to dynamical effects related to the location of the molecular gas in the inner region, on the rising part of the rotation curve, where shear is high. Although here the star formation per unit gas mass is reduced with respect to that observed in gas-rich rotating spirals, the number of stars that formed per free-fall time is constant (Davis et al. 2014). This result might be tightly connected to the more general morphological quenching scenario proposed by Martig et al. (2009), according to which gas discs can be stabilised against star formation when they are embedded in prominent bulges such as those observed in lenticular galaxies (see, however, Koyama et al. 2019). Although our results are in line with these interpretations, we caution that the star formation rates and the molecular gas column densities used in Fig. 21 might include systematic effects in the dust attenuation correction, which is highly uncertain whenever 2D Balmer decrement maps are not available (NGC 4429, NGC 4459, and NGC 4476), and in the assumed CO(3–2)/CO(1–0) (NGC 4429) and CO(2–1)/CO(1–0) (NGC 4459 and NGC 4476) flux ratios, which are still poorly constrained in these extreme environments. We can also add that the claimed low star formation efficiency strongly depends on the assumed CO-to-H_2 (X_{CO}) conversion factor, which is known to depend on the physical properties of the interstellar medium (e.g. Boselli et al. 1997; Kaufman et al. 1999; Bolatto et al. 2013). These discs are metal rich, dense in molecular gas, and are very dusty. They are thus typical environments in which self-shielding against the surrounding ISRF, which is mainly dominated by the emission of the evolved stellar population of the prominent bulges, is very efficient. In these environments, X_{CO} is expected to decrease, as suggested by models (Wolfire et al. 1995; Kaufman et al. 1999) and observations (Boselli et al. 2002; Bolatto et al. 2013). Furthermore, hot X-ray emitting gas is also present in some of these quiescent massive objects (NGC 4459, 4477, 4526, and 4552). It is thus conceivable that the X_{CO} conversion factor is systematically different than the one measured in the discs of massive star-forming spirals. This might explain the observed decrease in star formation efficiency by a factor of ∼2.5 in these inner discs of massive lenticular galaxies.

5. Discussion and conclusion

The VESTIGE Hα NB imaging survey has revealed eight massive ($10^{10} \lesssim M_{star} \lesssim 10^{11}\, M_\odot$) lenticular galaxies in the Virgo cluster with ionised gas emission in their inner (a few kiloparsec) regions. The ionised gas is generally located in a disc with a morphology very similar to that of the dust seen in absorption in the high-resolution HST images, as observed in other lenticular galaxies (e.g. Goudfrooij et al. 1994; Sarzi et al. 2006; Finkelman et al. 2010, 2012; Kulkarni et al. 2014). The filamentary structure of the ionised gas in two galaxies is similar to that observed in cooling flows at the centre of massive clusters. These eight objects are a significant fraction (∼25%) of the lenticular galaxies of the Virgo cluster in the same stellar mass range. Because the VESTIGE survey is still incomplete with a partial coverage of the VCC footprints (∼60%, with full depth only in ∼25% of the VCC), this work suggests that these ionised gas features are quite common in this cluster environment. The presence of ionised gas in early-type galaxies, and in particular in lenticular galaxies, has been known since the works of Pogge & Eskridge (1987, 1993), Trinchieri & di Serego Alighieri (1991), and Macchetto et al. (1996), but it has never been studied in such a detail due to the lack of high-resolution multifrequency data such as those presented here. The increase in image quality reached by the VESTIGE data with respect to those gathered by previous works using 2 m class telescopes, for which data for a few galaxies in common are available (e.g. Gavazzi et al. 2018b), is also remarkable. This is possible through the extraordinary seeing conditions at the CFHT, combined with the accurate stellar continuum subtraction based on broad-band colour images.

The analysis presented in this work has clearly shown that in most cases, the gas is photoionised by young stars that are newly formed in the disc. These results suggest that this Virgo cluster sample is significantly different from the ATLAS^{3D} sample, in which the gas is mostly ionised by evolved stars and only in 10% of them by young stars (Sarzi et al. 2010). Systematic differences between cluster and isolated systems are expected, however, as is indeed observed in their kinematical (e.g. Davis et al. 2011; Krajnović et al. 2011) and dust versus gas properties (Kokusho et al. 2019). In these Virgo galaxies, the Hα luminosity is a direct tracer of star formation and indicates that these objects lie well below the main-sequence relation driven by normal star-forming discs, with star formation rates of about $0.02 \lesssim \mathrm{SFR} \lesssim 0.15\, M_\odot\, \mathrm{yr}^{-1}$. We also derived the statistical properties of individual HII regions detected in these star-forming discs, showing that they correspond to those encountered in normal star-forming galaxies on average. In NGC 4262 and NGC 4552, where the emission is principally due to filamentary structures, the gas is probably shock ionised and might be hot gas that is cooling and infalling into the nucleus after a merging event. The lack of strong AGNs causes us to exclude nuclear activity as the main source of ionisation in all the targets.

CO millimetric CARMA and ALMA data allowed us to show that the total molecular gas content of these objects ($2 \times 10^7 \lesssim M(H_2) \lesssim 5 \times 10^8\, M_\odot$) is lower than that found in spiral galaxies of similar mass (e.g. Boselli et al. 2014c). The molecular gas is distributed within discs with properties similar to those observed in Hα, and forms stars following the Schmidt relation, but with an efficiency ≃2.5 lower than that observed in spiral galaxies, as previously found in similar objects by Davis et al. (2014). The low star formation efficiency observed in these systems might be due to a variation in the shear or in the global stability of the gas, which is here located in the inner regions, where the rotation curve of the galaxies rises rapidly (Davis et al. 2014) and the gas becomes supported by pressure (Bertola et al. 1995).

Optical (HST and NGVS) and far-IR (*Herschel* and *Spitzer*) images both indicate amounts of dust in these lenticular galaxies, as is often observed in early-type systems (e.g. Goudfrooij & de Jong 1995). The multifrequency data allowed us to estimate their total dust content using two independent techniques. The first technique is based on the SED fitting analysis including UV-to-far-IR data. The second technique is based on the measure of the optical attenuation derived from the NGVS broad-band images after subtracting a model to trace the intrinsic distribution of stars. The two techniques give very different results, with the SED fitting analysis providing dust masses ∼100

times higher than those obtained from the 2D dust attenuation maps. The comparison of the *Herschel*/PACS 100 μm image of NGC 4526 with the Balmer decrement map obtained using the MUSE data convolved to a similar resolution has indicated a similar distribution of the emitting and absorbing dust in this galaxy. This result thus excludes any major contribution of diffuse dust locked up in the atmosphere of evolved stars, which might be missed in the visible 2D dust attenuation maps as the origin of this major discrepancy. This analysis suggests that the 2D dust attenuation maps derived from the optical images strongly underestimate the total dust content of these lenticular galaxies just because only a fraction of the stellar emission, which is geometrically located along the line of sight behind the dust screen, is efficiently absorbed by dust. This result agrees with the result found by the radiation transfer analysis of two early-type galaxy in the Virgo and Fornax clusters with similar properties (Viaene et al. 2015, 2019). Again, the total dust mass of these galaxies, which ranges between $6 \times 10^5 \lesssim M_{\rm dust} \lesssim 10^7\,M_\odot$, is fairly low compared to that of spiral galaxies of similar stellar mass (e.g. Cortese et al. 2012). However, it matches the typical dust mass of lenticulars estimated using *Herschel* data from the *Herschel* Reference Survey (Smith et al. 2012).

While in a few objects, the origin of the ionised gas seems clear, in others, the multifrequency data give contradictory results. In NGC 4262 and NGC 4552, the filamentary structure of the ionised gas, the presence of a cold gas and young stellar ring misaligned with the stellar main body of the galaxy (NGC 4262), and the prominent shells and tidal tails in the deep NGVS broad-band optical images (NGC 4552) clearly suggest an external origin of the gas, which must have been accreted after a merging event. NGC 4262 is an S0 galaxy with a gaseous ring, which hydrodynamic simulations indicate might have been formed after a minor merging event with a gas-rich spiral galaxy (Mapelli et al. 2015). NGC 4552 is a slow rotator and might have been formed after a major merging episode that was able to heat the stellar disc and produce typical gravitation perturbations such as those seen in the optical image (Penoyre et al. 2017; Pop et al. 2018). In these objects, gas and dust might have been accreted after a strong gravitational interaction with a gas-rich system. When it is in contact with the hot coronal gas that emits in X-rays, the cold accreted gas is heated and becomes ionised, while the dust remains shielded within the stripped cold gas, which gradually evaporates (evaporation flow scenario; Sparks et al. 1989, de Jong et al. 1990, Finkelman et al. 2012). This scenario predicts that the ionised gas and the dust are located in similar filamentary structures as are observed in these two galaxies.

MUSE spectroscopic data of NGC 4469 and NGC 4526 have shown that the typical metallicity of the gas over the star-forming discs is about solar, as expected for these massive galaxies. The analysis presented in Sect. 4 has also shown that most of the galaxies have a gas-to-dust ratio of $G/D \simeq 80$, typical of star-forming systems of similar stellar mass (e.g. Rémy-Ruyer et al. 2014). As extensively discussed in Davis et al. (2011), this evidence suggests that the gas has an internal origin and might be either recycled gas produced by the old stellar population that dominates in these early-type systems, or the remnant of gas that is locked up in the inner regions in star-forming galaxies that are stripped of their ISM by a ram pressure stripping event (e.g. Boselli & Gavazzi 2006; Boselli et al. 2021a). The first hypothesis (gas produced by stellar mass loss), however, is questioned because the amount of associated dust is too low compared to that observed in these early-type systems (Patil et al. 2007). Ram pressure stripping removes the gas outside-in, producing radially truncated discs because the gas is hardly perturbed in the inner regions where the gravitational potential well of the galaxy is sufficiently deep to keep it anchored to the disc (e.g. Boselli et al. 2006). Evidence of an ongoing ram pressure stripping event is present in NGC 4469, which has a prominent tail of ionised gas emitted from the disc without any stellar counterpart. This is typical of galaxies undergoing this perturbing mechanism (e.g. Boselli et al. 2021a). Similar features, although observed with a much lower angular resolution in the X-rays images, are also present in NGC 4477 and NGC 4552, suggesting that ram pressure is perturbing the gas in the outer halo of these objects (Li et al. 2018; Machacek et al. 2006b). Recently accreted gas via infall or minor merging events would be unpolluted or low-metallicity gas and would therefore have different properties than those that are observed in most of these objects.

Indications about the possible origin of the ionised gas can be taken from the analysis of the 2D stellar distribution and of the relative kinematics of the gas and of the stars. As mentioned above, the merging origin of NGC 4552 is clear. It is suggested by the deep NGVS broad-band image, which shows prominent shells and tidal remnants. In this object, the gas has been accreted during a merging event, but its observed distribution is also affected by an ongoing ram pressure stripping episode. Another interesting example is the X-shaped, boxy stellar morphology with a tilted outer disc of NGC 4469. This peculiar morphology has been interpreted as a possible result of harassment (Mosenkov et al. 2020), or of a recent merging event (Mihos et al. 1995), although the ionised gas tail SW of the galaxy due to a ram pressure stripping event is further evidence that different mechanisms can act simultaneously. Three out of eight galaxies (NGC 4262, 4469, and 4477) have a prominent bar, which often indicates a recent instability of the stellar disc resulting from strong gravitational perturbation (e.g. Moore et al. 1998). An external origin of the ionised gas (gas accretion, minor merger) is also suggested by the misalignement of the stellar and ionised gas kinematics observed in NGC 4477 (Sarzi et al. 2006; Crocker et al. 2011) or by the peculiar stellar kinematics of NGC 4429 (Cortés et al. 2015) and NGC 4526 (Sarzi et al. 2006; Krajnović et al. 2011; Foster et al. 2016. In contrast, Bertola et al. (1995) interpreted the high-velocity dispersion of the ionised gas observed in some lenticular galaxies as an indication that this gas has been produced from the mass lost by evolved stars in the bulge.

All these physical properties derived from the analysis of each single object should be considered along with more general arguments based on the expected evolution of these lenticular galaxies within the Virgo cluster environment. This can be done by tracing their position within the phase-space diagram (see Fig. 16), as has been done for these and other objects in Boselli et al. (2014a, 2016b) (see also Cortese et al. 2021). Figure 16 clearly shows that most if not all of these lenticulars are located within the intermediate region composed of objects accreted by the cluster $3.6 < \tau_{\rm inf} < 6.5$ Gyr ago, as indicated by the simulations of Rhee et al. (2017). These timescales are slightly longer than those derived from the SED fitting analysis of Boselli et al. (2016b) for the quenching of the star formation activity of early-type galaxies within the Virgo cluster ($1 \lesssim \tau_{\rm quench} \lesssim 3$ Gyr), consistent with a picture according to which these lenticular galaxies are accreted as gas-rich systems and later quench their star formation activity after their interaction with the hostile surrounding environment.

Despite the exquisite quality of the multifrequency data we used and our analysis, we are unable to identify a unique origin for the ionised gas in these eight lenticular galaxies that

are located within the Virgo cluster. This result is due to the fact that lenticular galaxies in rich environments have been formed following different formation paths because they might have encountered several perturbing mechanisms that worked together to different degrees and affected their star formation history in a complex and unpredictable way. This is also the case for the galaxies we analysed here. For this reason, we plan to study the structural and kinematical properties of the stars and of the gas in detail, using the unique set of available mutlifrequency data or data gathered with targeted IFU spectroscopic observations that were undertaken recently at the Observatoire de Haute-Provence. We also plan to use the complete VESTIGE blind survey to statistically quantify the frequency of these objects in a cluster such as Virgo, and compare it to the predictions of semi-analytic models and simulations (e.g. Lagos et al. 2014). The results of these analyses will be presented in forthcoming communications.

Acknowledgements. We are grateful to the whole CFHT team who assisted us in the preparation and in the execution of the observations and in the calibration and data reduction: Todd Burdullis, Daniel Devost, Bill Mahoney, Nadine Manset, Andreea Petric, Simon Prunet, Kanoa Withington. We also thank S. Torres and the SOAR team for their support during the observations and data reduction, and the referee for constructive comments and suggestions. We acknowledge financial support from "Programme National de Cosmologie and Galaxies" (PNCG) funded by CNRS/INSU-IN2P3-INP, CEA and CNES, France, and from "Projet International de Coopération Scientifique" (PICS) with Canada funded by the CNRS, France. This research has made use of the NASA/IPAC Extragalactic Database (NED) which is operated by the Jet Propulsion Laboratory, California Institute of Technology, under contract with the National Aeronautics and Space Administration and of the GOLDMine database (http://goldmine.mib.infn.it/) (Gavazzi et al. 2003). The UVIT project is collaboration between the following institutes from India: Indian Institute of Astrophysics (IIA), Bengaluru, Inter University Centre for Astronomy and Astrophysics (IUCAA), Pune, and National Centre for Radioastrophysics (NCRA) (TIFR), Pune, and the Canadian Space Agency (CSA). This paper makes use of the following ALMA data: ADS/JAO.ALMA 2013.1.00493.S. ALMA is a partnership of ESO (representing its member states), NSF (USA) and NINS (Japan), together with NRC (Canada), MOST and ASIAA (Taiwan), and KASI (Republic of Korea), in cooperation with the Republic of Chile. The Joint ALMA Observatory is operated by ESO, AUI/NRAO and NAOJ. The National Radio Astronomy Observatory is a facility of the National Science Foundation operated under cooperative agreement by Associated Universities, Inc. M.F. has received funding from the European Research Council (ERC) (grant agreement No 757535). N.Z.D. acknowledges partial support from FONDECYT through project 3190769. L.G. acknowledges financial support from the Spanish Ministry of Science and Innovation (MCIN) under the 2019 Ramón y Cajal program RYC2019-027683 and from the Spanish MCIN project HOSTFLOWS PID2020-115253GA-I00. M.B. gratefully acknowledges support by the ANID BASAL project FB210003 and the FONDECYT regular grant 1211000. L.C. acknowledges support from the Australian Research Council Discovery Project and Future Fellowship funding schemes (DP210100337, FT180100066). Parts of this research were conducted by the Australian Research Council Centre of Excellence for All Sky Astrophysics in 3 Dimensions (ASTRO 3D), through project number CE170100013.

References

Agrawal, P. C. 2006, Adv. Space Res., 38, 2989
Alatalo, K., Davis, T. A., Bureau, M., et al. 2013, MNRAS, 432, 1796
Annibali, F., Bressan, A., Rampazzo, R., et al. 2010, A&A, 519, A40
Asplund, M., Grevesse, N., Sauval, A. J., et al. 2009, ARA&A, 47, 481
Auld, R., Bianchi, S., Smith, M. W. L., et al. 2013, MNRAS, 428, 1880
Bamford, S. P., Nichol, R. C., Baldry, I. K., et al. 2009, MNRAS, 393, 1324
Bekki, K. 1998, ApJ, 502, L133
Bekki, K., & Couch, W. J. 2011, MNRAS, 415, 1783
Bekki, K., Couch, W. J., & Shioya, Y. 2002, ApJ, 577, 651
Bellstedt, S., Forbes, D. A., Foster, C., et al. 2017, MNRAS, 467, 4540
Bendo, G. J., Galliano, F., & Madden, S. C. 2012a, MNRAS, 423, 197
Bendo, G. J., Boselli, A., Dariush, A., et al. 2012b, MNRAS, 419, 1833
Bendo, G. J., Baes, M., Bianchi, S., et al. 2015, MNRAS, 448, 135
Bertola, F., Cinzano, P., Corsini, E. M., et al. 1995, ApJ, 448, L13
Bettoni, D., Buson, L. M., & Galletta, G. 2010, A&A, 519, A72
Bigiel, F., Leroy, A., Walter, F., et al. 2008, AJ, 136, 2846
Binggeli, B., Sandage, A., & Tammann, G. A. 1985, AJ, 90, 1681
Bocchio, M., Bianchi, S., & Abergel, A. 2016, A&A, 591, A117
Bolatto, A. D., Wolfire, M., & Leroy, A. K. 2013, ARA&A, 51, 207
Boquien, M., Burgarella, D., Roehlly, Y., et al. 2019, A&A, 622, A103
Boselli, A. 2011, A Panchromatic View of Galaxies (Berlin: Wiley-VCH), 324
Boselli, A., & Gavazzi, G. 2006, PASP, 118, 517
Boselli, A., & Gavazzi, G. 2014, A&ARv, 22, 74
Boselli, A., Gavazzi, G., Lequeux, J., et al. 1997, A&A, 327, 522
Boselli, A., Lequeux, J., Sauvage, M., et al. 1998, A&A, 335, 53
Boselli, A., Lequeux, J., & Gavazzi, G. 2002, A&A, 384, 33
Boselli, A., Cortese, L., Deharveng, J. M., et al. 2005, ApJ, 629, L29
Boselli, A., Boissier, S., Cortese, L., et al. 2006, ApJ, 651, 811
Boselli, A., Boissier, S., Cortese, L., et al. 2009, ApJ, 706, 1527
Boselli, A., Eales, S., Cortese, L., et al. 2010a, PASP, 122, 261
Boselli, A., Ciesla, L., Buat, V., et al. 2010b, A&A, 518, L61
Boselli, A., Boissier, S., Heinis, S., et al. 2011, A&A, 528, A107
Boselli, A., Ciesla, L., Cortese, L., et al. 2012, A&A, 540, A54
Boselli, A., Hughes, T. M., Cortese, L., Gavazzi, G., & Buat, V. 2013, A&A, 550, A114
Boselli, A., Voyer, E., Boissier, S., et al. 2014a, A&A, 570, A69
Boselli, A., Cortese, L., & Boquien, M. 2014b, A&A, 564, A65
Boselli, A., Cortese, L., Boquien, M., et al. 2014c, A&A, 564, A66
Boselli, A., Fossati, M., Gavazzi, G., et al. 2015, A&A, 579, A102
Boselli, A., Cuillandre, J. C., Fossati, M., et al. 2016a, A&A, 587, A68
Boselli, A., Roehlly, Y., Fossati, M., et al. 2016b, A&A, 596, A11
Boselli, A., Fossati, M., Ferrarese, L., et al. 2018a, A&A, 614, A56
Boselli, A., Fossati, M., Cuillandre, J. C., et al. 2018b, A&A, 615, A114
Boselli, A., Fossati, M., Consolandi, G., et al. 2018c, A&A, 620, A164
Boselli, A., Fossati, M., Longobardi, A., et al. 2019, A&A, 623, A52
Boselli, A., Fossati, M., Longobardi, A., et al. 2020, A&A, 634, L1
Boselli, A., Fossati, M., & Sun, M. 2021a, A&ARv, submitted [arXiv:2109.13614]
Boselli, A., Lupi, A., Epinat, B., et al. 2021b, A&A, 646, A139
Bournaud, F. 2016, Galactic Bulges, 355
Bournaud, F., Elmegreen, B. G., & Elmegreen, D. M. 2007, ApJ, 670, 237
Bournaud, F., Chapon, D., Teyssier, R., et al. 2011, ApJ, 730, 4
Bruzual, G., & Charlot, S. 2003, MNRAS, 344, 1000
Burstein, D. 1979, ApJ, 234, 435
Burstein, D., Ho, L. C., Huchra, J. P., et al. 2005, ApJ, 621, 246
Byrd, G., & Valtonen, M. 1990, ApJ, 350, 89
Calzetti, D., Armus, L., Bohlin, R. C., et al. 2000, ApJ, 533, 682
Calzetti, D., Kennicutt, R. C., Engelbracht, C. W., et al. 2007, ApJ, 666, 870
Calzetti, D., Wu, S.-Y., Hong, S., et al. 2010, ApJ, 714, 1256
Cappellari, M., Emsellem, E., Krajnović, D., et al. 2011, MNRAS, 413, 813
Chabrier, G. 2003, PASP, 115, 763
Ciesla, L., Boselli, A., Smith, M. W. L., et al. 2012, A&A, 543, A161
Ciesla, L., Boquien, M., Boselli, A., et al. 2014, A&A, 565, A128
Clemens, J. C., Crain, J. A., & Anderson, R. 2004, Proc. SPIE, 5492, 331
Combes, F., Young, L. M., & Bureau, M. 2007, MNRAS, 377, 1795
Conselice, C. J., Gallagher, J. S., III, & Wyse, R. F. G. 2001, AJ, 122, 2281
Consolandi, G., Gavazzi, G., Fossati, M., et al. 2017, A&A, 606, A83
Cortés, J. R., Kenney, J. D. P., & Hardy, E. 2015, ApJS, 216, 9
Cortese, L., Ciesla, L., Boselli, A., et al. 2012, A&A, 540, A52
Cortese, L., Fritz, J., Bianchi, S., et al. 2014, MNRAS, 440, 942
Cortese, L., Catinella, B., & Smith, R. 2021, PASA, 36, 35
Côté, P., Blakeslee, J. P., Ferrarese, L., et al. 2004, ApJS, 153, 223
Crocker, A. F., Bureau, M., Young, L. M., & Combes, F. 2011, MNRAS, 410, 1197
Curti, M., Cresci, G., Mannucci, F., et al. 2017, MNRAS, 465, 1384
Dame, T. M., Hartmann, D., & Thaddeus, P. 2001, ApJ, 547, 792
Davies, J. I., Baes, M., Bendo, G. J., et al. 2010, A&A, 518, L48
Davis, T. A., Alatalo, K., Sarzi, M., et al. 2011, MNRAS, 417, 882
Davis, T. A., Alatalo, K., Bureau, M., et al. 2013, MNRAS, 429, 534
Davis, T. A., Young, L. M., Crocker, A. F., et al. 2014, MNRAS, 444, 3427
Davis, T. A., Rowlands, K., Allison, J. R., et al. 2015, MNRAS, 449, 3503
Davis, T. A., Bureau, M., Onishi, K., et al. 2018, MNRAS, 473, 3818
Davis, T. A., Greene, J. E., Ma, C.-P., et al. 2019, MNRAS, 486, 1404
de Jong, T., Norgaard-Nielsen, H. U., Jorgensen, H. E., & Hansen, L. 1990, A&A, 232, 317
Diaz, J., Bekki, K., Forbes, D. A., et al. 2018, MNRAS, 477, 2030
Domínguez Sánchez, H., Huertas-Company, M., Bernardi, M., et al. 2018, MNRAS, 476, 3661
Draine, B. T. 2003, ARA&A, 41, 241
Draine, B. T., & Li, A. 2007, ApJ, 657, 810
Draine, B. T., Dale, D. A., Bendo, G., et al. 2007, ApJ, 663, 866
Dressler, A. 1980, ApJ, 236, 351
Dressler, A. 2004, Clusters of Galaxies: Probes of Cosmological Structure and Galaxy Evolution, 206

Dressler, A., & Sandage, A. 1983, ApJ, 265, 664
Dressler, A., Oemler, A., Jr, Couch, W. J., et al. 1997, ApJ, 490, 577
Dwek, E. 1998, ApJ, 501, 643
Eliche-Moral, M. C., Rodríguez-Pérez, C., Borlaff, A., et al. 2018, A&A, 617, A113
Ellison, S. L., Lin, L., Thorp, M. D., et al. 2021, MNRAS, 501, 4777
Emsellem, E., Cappellari, M., Krajnović, D., et al. 2011, MNRAS, 414, 888
Erwin, P., Gutiérrez, L., & Beckman, J. E. 2012, ApJ, 744, L11
Erwin, P., Saglia, R. P., Fabricius, M., et al. 2015, MNRAS, 446, 4039
Ferrarese, L., Côté, P., Cuillandre, J.-C., et al. 2012, ApJS, 200, 4
Finkelman, I., Brosch, N., Funes, J. G., et al. 2010, MNRAS, 407, 2475
Finkelman, I., Brosch, N., Funes, J. G., et al. 2012, MNRAS, 422, 1384
Fossati, M., Fumagalli, M., Boselli, A., et al. 2016, MNRAS, 455, 2028
Fossati, M., Mendel, J. T., Boselli, A., et al. 2018, A&A, 614, A57
Fossati, M., Fumagalli, M., Gavazzi, G., et al. 2019, MNRAS, 484, 2212
Foster, C., Pastorello, N., Roediger, J., et al. 2016, MNRAS, 457, 147
Fraser-McKelvie, A., Aragón-Salamanca, A., Merrifield, M., et al. 2018, MNRAS, 481, 5580
Friedli, D., & Martinet, L. 1993, A&A, 277, 27
Gadotti, D. A. 2012, ArXiv eprints [arXiv:1208.2295]
Galbany, L., Anderson, J. P., Rosales-Ortega, F. F., et al. 2016, MNRAS, 455, 4087
Gavazzi, G., Boselli, A., Scodeggio, M., Pierini, D., & Belsole, E. 1999, MNRAS, 304, 595
Gavazzi, G., Boselli, A., Vílchez, J. M., Iglesias-Paramo, J., & Bonfanti, C. 2000, A&A, 361, 1
Gavazzi, G., Boselli, A., Donati, A., Franzetti, P., & Scodeggio, M. 2003, A&A, 400, 451
Gavazzi, G., Zaccardo, A., Sanvito, G., Boselli, A., & Bonfanti, C. 2004, A&A, 417, 499
Gavazzi, G., Consolandi, G., Belladitta, S., et al. 2018a, A&A, 615, A104
Gavazzi, G., Consolandi, G., Pedraglio, S., et al. 2018b, A&A, 611, A28
Geach, J. E., Smail, I., Moran, S. M., et al. 2009, ApJ, 691, 783
Giannetti, A., Leurini, S., König, C., et al. 2017, A&A, 606, L12
Giovanelli, R., Haynes, M. P., Kent, B. R., et al. 2005, AJ, 130, 2598
Goudfrooij, P., & de Jong, T. 1995, A&A, 298, 784
Goudfrooij, P., Hansen, L., Jorgensen, H. E., et al. 1994, A&AS, 105, 341
Gwyn, S. D. J. 2008, PASP, 120, 212
Hafok, H., & Stutzki, J. 2003, A&A, 398, 959
Haynes, M. P., Giovanelli, R., Kent, B. R., et al. 2018, ApJ, 861, 49
Helmboldt, J. F., Walterbos, R. A. M., Bothun, G. D., et al. 2005, ApJ, 630, 824
Ho, L. C., Filippenko, A. V., & Sargent, W. L. W. 1997, ApJS, 112, 315
Hou, M., Li, Z., Jones, C., et al. 2021, ApJ, 919, 141
Hubble, E. P. 1936, Realm of the Nebulae (New Haven: Yale University Press), 1936
Issa, M. R., MacLaren, I., & Wolfendale, A. W. 1990, A&A, 236, 237
Junais, Boissier, A., Boselli, M., et al. 2021, A&A, 650, A99
Kauffmann, G., Heckman, T. M., Tremonti, C., et al. 2003, MNRAS, 346, 1055
Kaufman, M. J., Wolfire, M. G., Hollenbach, D. J., & Luhman, M. L. 1999, ApJ, 527, 795
Kennicutt, R. C., Jr 1998a, ARA&A, 36, 189
Kennicutt, R. C. 1998b, ApJ, 498, 541
Kewley, L. J., Dopita, M. A., Sutherland, R. S., Heisler, C. A., & Trevena, J. 2001, ApJ, 556, 121
Kewley, L. J., Groves, B., Kauffmann, G., & Heckman, T. 2006, MNRAS, 372, 961
Kim, D.-W., Anderson, C., Burke, D., et al. 2019, ApJS, 241, 36
Kitayama, T., Ito, Y., Okada, Y., et al. 2009, ApJ, 695, 1191
Kokusho, T., Kaneda, H., Bureau, M., et al. 2019, A&A, 622, A87
Koyama, S., Koyama, Y., Yamashita, T., et al. 2019, ApJ, 874, 142
Kraft, R. P., Roediger, E., Machacek, M., et al. 2017, ApJ, 848, 27
Krajnović, D., Cappellari, M., de Zeeuw, P. T., et al. 2006, MNRAS, 366, 787
Krajnović, D., Emsellem, E., Cappellari, M., et al. 2011, MNRAS, 414, 2923
Krumm, N., van Driel, W., & van Woerden, H. 1985, A&A, 144, 202
Kulkarni, S., Sahu, D. K., Chaware, L., et al. 2014, New Astron., 30, 51
Lagos, C. P., Davis, T. A., Lacey, C. G., et al. 2014, MNRAS, 443, 1002
Lapham, R. C., & Young, L. M. 2019, ApJ, 875, 3
Larson, R. B., Tinsley, B. M., & Caldwell, C. N. 1980, ApJ, 237, 692
Laurikainen, E., Salo, H., & Buta, R. 2005, MNRAS, 362, 1319
Laurikainen, E., Salo, H., Buta, R., et al. 2006, AJ, 132, 2634
Leroy, A. K., Walter, F., Bigiel, F., et al. 2009, AJ, 137, 4670
Leroy, A. K., Rosolowsky, E., Usero, A., et al. 2021, ApJ, submitted [arXiv:2109.11583]
Li, Y., Su, Y., & Jones, C. 2018, MNRAS, 480, 4279
Longobardi, A., Boselli, A., Fossati, M., et al. 2020, A&A, 644, A161
Lucero, D. M., & Young, L. M. 2013, AJ, 145, 56
Lucero, D. M., Young, L. M., & van Gorkom, J. H. 2005, AJ, 129, 647
Macchetto, F., Pastoriza, M., Caon, N., et al. 1996, A&AS, 120, 463
Machacek, M., Jones, C., Forman, W. R., & Nulsen, P. 2006a, ApJ, 644, 155
Machacek, M., Nulsen, P. E. J., Jones, C., & Forman, W. R. 2006b, ApJ, 648, 947
Mapelli, M., Rampazzo, R., & Marino, A. 2015, A&A, 575, A16
Martig, M., Bournaud, F., Teyssier, R., et al. 2009, ApJ, 707, 250
Maschmann, D., Melchior, A.-L., Mamon, G. A., et al. 2020, A&A, 641, A171
Masters, K. L., Mosleh, M., Romer, A. K., et al. 2010, MNRAS, 405, 783
Mattsson, L., & Andersen, A. C. 2012, MNRAS, 423, 38
Mattsson, L., De Cia, A., Andersen, A. C., et al. 2014, MNRAS, 440, 1562
McDonald, M., Veilleux, S., Rupke, D. S. N., & Mushotzky, R. 2010, ApJ, 721, 1262
McDonald, M., Veilleux, S., & Rupke, D. S. N. 2012, ApJ, 746, 153
McMullin, J. P., Waters, B., Schiebel, D., et al. 2007, Astron. Data Anal. Softw. Syst. XVI, 376, 127
Mei, S., Blakeslee, J. P., Côté, P., et al. 2007, ApJ, 655, 144
Méndez-Abreu, J., Aguerri, J. A. L., Falcón-Barroso, J., et al. 2018, MNRAS, 474, 1307
Mihos, J. C., Walker, I. R., Hernquist, L., et al. 1995, ApJ, 447, L87
Moore, B., Katz, N., Lake, G., et al. 1996, Nature, 379, 613
Moore, B., Lake, G., & Katz, N. 1998, ApJ, 495, 139
Morganti, R., de Zeeuw, P. T., Oosterloo, T. A., et al. 2006, MNRAS, 371, 157
Mosenkov, A. V., Smirnov, A. A., Sil'chenko, O. K., et al. 2020, MNRAS, 497, 2039
Noll, S., Burgarella, D., Giovannoli, E., et al. 2009, A&A, 507, 1793
O'Connell, R. W. 1999, ARA&A, 37, 603
Oosterloo, T., Morganti, R., Crocker, A., et al. 2010, MNRAS, 409, 500
Osterbrock, D. E., & Ferland, G. J. 2006, Astrophysics of Gaseous Nebulae and Active Galactic Nuclei (Sausalito, CA: University Science Books), 2006
Panuzzo, P., Rampazzo, R., Bressan, A., et al. 2011, A&A, 528, A10
Patil, M. K., Pandey, S. K., Sahu, D. K., et al. 2007, A&A, 461, 103
Penoyre, Z., Moster, B. P., Sijacki, D., et al. 2017, MNRAS, 468, 3883
Pogge, R. W., & Eskridge, P. B. 1987, AJ, 93, 291
Pogge, R. W., & Eskridge, P. B. 1993, AJ, 106, 1405
Poggianti, B. M., Smail, I., Dressler, A., et al. 1999, ApJ, 518, 576
Poggianti, B. M., Bridges, T. J., Komiyama, Y., et al. 2004, ApJ, 601, 197
Poggianti, B. M., Fasano, G., Bettoni, D., et al. 2009, ApJ, 697, L137
Pop, A.-R., Pillepich, A., Amorisco, N. C., et al. 2018, MNRAS, 480, 1715
Proxauf, B., Öttl, S., & Kimeswenger, S. 2014, A&A, 561, A10
Quilis, V., Moore, B., & Bower, R. 2000, Science, 288, 1617
Rémy-Ruyer, A., Madden, S. C., Galliano, F., et al. 2014, A&A, 563, A31
Rhee, J., Smith, R., Choi, H., et al. 2017, ApJ, 843, 128
Rich, J. A., Kewley, L. J., & Dopita, M. A. 2011, ApJ, 734, 87
Rieke, G. H., Young, E. T., Engelbracht, C. W., et al. 2004, ApJS, 154, 25
Rizzo, F., Fraternali, F., & Iorio, G. 2018, MNRAS, 476, 2137
Roediger, E., Kraft, R. P., Nulsen, P. E. J., et al. 2015, ApJ, 806, 104
Roman-Duval, J., Gordon, K. D., Meixner, M., et al. 2014, ApJ, 797, 86
Rousseau-Nepton, L., Robert, C., Martin, R. P., Drissen, L., & Martin, T. 2018, MNRAS, 477, 4152
Sage, L. J., & Wrobel, J. M. 1989, ApJ, 344, 204
Sandage, A., & Visvanathan, N. 1978a, ApJ, 223, 707
Sandage, A., & Visvanathan, N. 1978b, ApJ, 225, 742
Sandage, A., Binggeli, B., & Tammann, G. A. 1985, AJ, 90, 1759
Sandstrom, K. M., Leroy, A. K., Walter, F., et al. 2013, ApJ, 777, 5
Sardaneta, M. M., Amram, P., Boselli, A., et al. 2022, A&A, 659, A45
Sarzi, M., Falcón-Barroso, J., Davies, R. L., et al. 2006, MNRAS, 366, 1151
Sarzi, M., Shields, J. C., Schawinski, K., et al. 2010, MNRAS, 402, 2187
Schmidt, M. 1959, ApJ, 129, 243
Serra, P., Oosterloo, T., Morganti, R., et al. 2012, MNRAS, 422, 1835
Serra, P., Oser, L., Krajnović, D., et al. 2014, MNRAS, 444, 3388
Sharp, R. G., & Bland-Hawthorn, J. 2010, ApJ, 711, 818
Sil'chenko, O. K., & Afanasiev, V. L. 2002, A&A, 385, 1
Smith, M. W. L., Gomez, H. L., Eales, S. A., et al. 2012, ApJ, 748, 123
Sodroski, T. J., Bennett, C., Boggess, N., et al. 1994, ApJ, 428, 638
Sparks, W. B., Macchetto, F., & Golombek, D. 1989, ApJ, 345, 153
Spitzer, L. 1978, in A Wiley-Interscience Publication (New York: Wiley), 1978
Spitzer, L., & Baade, W. 1951, ApJ, 113, 413
Strong, A. W., Bloemen, J. B. G. M., Dame, T. M., et al. 1988, A&A, 207, 1
Su, Y., Irwin, J. A., White, R. E., et al. 2015, ApJ, 806, 156
Tandon, S. N., Postma, J., Joseph, P., et al. 2020, AJ, 159, 158
Tapia, T., Eliche-Moral, M. C., Aceves, H., et al. 2017, A&A, 604, A105
Temi, P., Brighenti, F., & Mathews, W. G. 2009, ApJ, 695, 1
Thilker, D. A., Braun, R., & Walterbos, R. A. M. 2000, AJ, 120, 3070
Thronson, H. A., Tacconi, L., Kenney, J., et al. 1989, ApJ, 344, 747
Triani, D. P., Sinha, M., Croton, D. J., et al. 2020, MNRAS, 493, 2490
Trinchieri, G., & di Serego Alighieri, S. 1991, AJ, 101, 1647
Utomo, D., Blitz, L., Davis, T., et al. 2015, ApJ, 803, 16
Valiante, R., Schneider, R., Bianchi, S., et al. 2009, MNRAS, 397, 1661

van den Bergh, S. 1976, ApJ, 206, 883
van den Bergh, S. 1990, ApJ, 348, 57
van den Bergh, S. 2009, ApJ, 702, 1502
van de Voort, F., Davis, T. A., Matsushita, S., et al. 2018, MNRAS, 476, 122
van Driel, W., & van Woerden, H. 1991, A&A, 243, 71
Vazdekis, A., Sánchez-Blázquez, P., Falcón-Barroso, J., et al. 2010, MNRAS, 404, 1639
Viaene, S., De Geyter, G., Baes, M., et al. 2015, A&A, 579, A103
Viaene, S., Sarzi, M., Zabel, N., et al. 2019, A&A, 622, A89
Visvanathan, N., & Sandage, A. 1977, ApJ, 216, 214
Vollmer, B., Fossati, M., Boselli, A., et al. 2021, A&A, 645, A121
Welch, G. A., & Sage, L. J. 2003, ApJ, 584, 260
Whitmore, B. C., Gilmore, D. M., & Jones, C. 1993, ApJ, 407, 489
Wilman, D. J., Oemler, A., Mulchaey, J. S., et al. 2009, ApJ, 692, 298
Wilson, C. D., Warren, B. E., Israel, F. P., et al. 2012, MNRAS, 424, 3050
Wolfire, M. G., Hollenbach, D., McKee, C. F., Tielens, A. G. G. M., & Bakes, E. L. O. 1995, ApJ, 443, 152
Wright, E. L., Eisenhardt, P. R. M., Mainzer, A. K., et al. 2010, AJ, 140, 1868
Yang, Y., Zabludoff, A. I., Zaritsky, D., et al. 2008, ApJ, 688, 945
Young, L. M. 2002, AJ, 124, 788
Young, L. M., Bureau, M., & Cappellari, M. 2008, ApJ, 676, 317
Young, L. M., Bureau, M., Davis, T. A., et al. 2011, MNRAS, 414, 940
Young, L. M., Scott, N., Serra, P., et al. 2014, MNRAS, 444, 3408
Zabludoff, A. I., Zaritsky, D., Lin, H., et al. 1996, ApJ, 466, 104
Zhukovska, S., Gail, H.-P., & Trieloff, M. 2008, A&A, 479, 453

Appendix A: Comments on individual objects

A.1. NGC4262 (VCC 355)

The Hα image of NGC 4262 (Fig. 1) shows an extended ring-like structure characterised by a few HII regions oriented along a NE-SW major axis. This ring-like structure is also visible in the ASTROSAT/UVIT FUV image (Fig. 2) and in the GALEX images (Bettoni et al. 2010). It signifies the presence of young stars. The ring has been also detected in HI by Krumm et al. (1985) and more recently by Oosterloo et al. (2010) with the WSRT. The thin HI ring structure, its orientation with respect to the main stellar disc (polar ring, Serra et al. 2014), and its extension (a factor of ~ 2 larger than the stellar disc) led Krumm et al. (1985) conclude that the HI gas ring is either the remnant of the primordial proto-galaxy cloud or HI gas recently accreted from the intergalactic medium or from a captured gas-rich dwarf. By studying the relative kinematics of the HI gas within the ring and that of the ionised gas in the inner regions, which is strongly kinematically decoupled from that of the stars within the disc (Sarzi et al. 2006), Bettoni et al. (2010) proposed that the atomic gas has been removed from the main body of the galaxy after a gravitational interaction with another Virgo cluster member, possibly NGC 4254. The NGVS (Fig. 5) and HST (Fig. 6) images indicate a prominent bar, whose origin is often associated with gravitational perturbations (e.g. Moore et al. 1996, 1998). Hydrodynamic simulations indicate that galaxies with gas-rich polar rings are generally formed after a minor merging event (Mapelli et al. 2015). All this observational evidence, combined with the evidence presented here, consistently suggests that NGC 4262 has recently been gravitationally perturbed. This is probably at the origin of the ionised gas filaments that are observed in the inner regions and of the HI gas in the polar ring structure.

A.2. NGC4429 (VCC1003)

NGC 4429 is characterised by a high surface brightness ionised gas disc located in the inner 0.47 kpc region (radius), and a more extended (1.1 kpc) low surface brightness disc (Fig. 1). A very similar morphology is visible in absorption in the HST F606W (Fig. 6) and NGVS (Fig. 17) images, which reveal a dust disc with a folded spiral structure associated with the ionised gas disc. The dust disc also contains cold rotating molecular gas (Alatalo et al. 2013; Davis et al. 2018). IFU spectroscopy of NGC 4429 shows a regular stellar velocity field, suggesting a pure circular motion with possibly a cold circumnuclear stellar disc (Cortés et al. 2015). The velocity dispersion pattern, however, is fairly asymmetric, again suggesting a circumnuclear disc (Cortés et al. 2015). The steeply rising rotation curve also suggests a high concentration of the central mass. NGC 4429 is classified as a fast rotator (Emsellem et al. 2011) despite its high central velocity dispersion ($\sigma \simeq 200$ km s^{-1}, Cortés et al. 2015). The galaxy also shows a kinematically distinct component, that is, with the stellar kinematic PA aligned with the photometric PA in the inner ($r \leq 2$ kpc) and outer galaxy, but misaligned by $\sim 10^{\circ}$ at intermediate radii (Cortés et al. 2015). These kinematical properties led Cortés et al. (2015) conclude that NGC 4429 might result from a minor (3:1-6:1) merger, where the gas has been accreted in the inner regions after this event.

A.3. NGC4459 (VCC1154)

NGC 4459 has an ionised gas disc in its inner region that corresponds to the dust disc observed in absorption in the HST F475W (Fig. 6) and NGVS (Fig. 17) images and to the molecular gas disc seen with ALMA. The high-resolution HST image shows that the dust is distributed in two concentric almost face-on discs with folded spiral structures. The same disc has tentatively been detected in HI by Lucero & Young (2013). Crocker et al. (2011) derived a star formation of $\simeq 0.05$-0.12 $M_{\odot}$ yr^{-1}, which is slightly higher than the star formation we measured (see Table 1). They also showed a surprisingly low radio continuum activity with respect to the galaxy far-infrared emission. The molecular gas kinematics (Young et al. 2008) does not give any strong indication about the possible origin of the gas because the gaseous disc is kinematically coupled with the rotating stellar disc. The stellar kinematics derived using SAURON indicates that the galaxy is a fast rotator (Sarzi et al. 2006) with regular stellar kinematics (Krajnović et al. 2006). The kinematics of the galaxy derived using globular clusters indicates that the high-velocity rotation is also conserved well outside the effective radius (Bellstedt et al. 2017). After a comparison with hydrodynamic simulations, Bellstedt et al. (2017) concluded that the kinematical properties of NGC 4459 are consistent with a gas-rich minor merger origin, although they did not exclude a major merging event. Our results, however, combined with the agreement between the stellar and gas kinematics, rather suggest an internal origin, with gas stripped in the outer disc by ram pressure. The same conclusion was obtained after the analysis of the X-ray morphology of the galaxy conducted by Hou et al. (2021).

A.4. NGC4469 (VCC1190)

NGC 4469 is an edge-on galaxy classified as a barred lenticular galaxy (see Table 1), with a typical boxy or peanut morphology (see Fig. 5). The Hα image shows a thin star-forming disc with filaments of ionised gas on the z-plane. The analysis of deep optical images of this galaxy revealed a tilted outer disc that has been interpreted by Mosenkov et al. 2020 as a possible result of harassment. This agrees with the scenario that the boxy morphology is caused by a recent gravitational instability (e.g. Gadotti 2012), although gas accretion of gas-rich satellites occurring several billion years ago cannot be ruled out. The X-shape of the bulge observed in this edge-on galaxy is another indication of a recent merger (Mihos et al. 1995). The ionised gas filament without any associated stellar counterpart we discovered rather suggests a ram pressure stripping event that was able to remove a large fraction of the cold gas from the outer regions, which produced a truncated disc. The shock-ionised gas observed in the z-plane has been probably ionised during its interaction with the surrounding intracluster medium.

A.5. NGC4476 (VCC1250)

The Hα image of NGC 4476 shows a central ring-like structure with prominent HII regions similar to those observed in spiral galaxies, although here limited to the very inner region. The HST F475W image shows that these star-forming regions are associated with a dusty disc with an evident spiral structure. The high H_2/HI molecular-to-atomic gas ratio compared to that observed in normal late-type galaxies led Lucero et al. 2005 to conclude that the observed gas disc of NGC 4476 is the result of a ram pressure stripping event. This perturbing mechanism has a differential effect that is able to remove the diffuse atomic gas more efficiently (this gas is mainly distributed in an extended disc) than the molecular gas component, which is mainly located in dense giant molecular clouds in the inner disc.

Young (2002) ruled out any possible internal origin of the gas, however, because its specific angular momentum is about three times higher than that of the stars. Our results are consistent with an internal origin of the gas. This would mean that it is the remnant of a ram pressure stripping event.

A.6. NGC4477 (VCC1253)

The Hα image of NGC 4477 reveals an ionised gas disc with spiral structures surrounding the nucleus (Fig. 1). The same disc is also visible in absorption in the HST F475W (Fig. 6) and in the NGVS (Fig. 17) images, although the dust is less spectacular than in other objects. This galaxy is also characterised by hot gas whose temperature decreases to $\sim$ 0.3 keV in the inner 2-3 kpc region (Li et al. 2018; Kim et al. 2019) in which the ionised gas disc is located. The hot gas is distributed along a spiral structure (Kim et al. 2019) with an asymmetric halo that probably formed by the gas stripped during the interaction with the surrounding ICM during the galaxy motion on the plane of the sky (Li et al. 2018). The X-ray observations seem to indicate that the galaxy experiences a feedback process due to the central AGN, which is able to produce two small cavities in the hot gas. The same observations suggests that the cold gas in the centre is accreted gas (Li et al. 2018). Plateau de Bure interferometric (PdBI) observations suggest that the molecular gas is located in a ring-like structure with kinematical properties similar to those of the ionised gas derived from the SAURON observations (Sarzi et al. 2006; Crocker et al. 2011). The difference between the stellar kinematics position angle and the ionised gas position angle is $\sim$ 30°, which might indicate an external origin of the gas (Sarzi et al. 2006; Crocker et al. 2011).

A.7. NGC4526 (VCC1535)

The Hα image shows a high surface brightness disc of ionised gas extending up to $\simeq$ 1.45 kpc (Fig. 1). The same disc is observed in absorption in the HST F475W (Fig. 6) and NGVS (Fig. 17) images and contains giant molecular clouds with properties similar to those observed in other late-type galaxies (Fig. 6; Utomo et al. 2015). The galaxy also has hot gas (0.3 keV) confined within the inner $\simeq$ 3 kpc, with a strong X-ray point source in the centre, although this has not been identified as a known AGN (Kim et al. 2019). *Herschel*/SPIRE spectroscopy indicates that the gas in the disc has a temperature of $T \simeq$ 15-20 K and an electron density of $n_e \simeq 1.6$ cm^{-2} (Lapham & Young 2019). This is significantly lower than the temperature derived using the [SII] doublet ratio (Fig. 9) or the size of the HII regions (Fig. 15). The stellar kinematics derived using the SAURON instrument (Sarzi et al. 2006; Krajnović et al. 2011) or with the spectroscopy of globular cluster in the outer regions (Foster et al. 2016) indicates that the galaxy is a fast rotator with a double-maximum velocity profile and regular gas kinematics. These kinematical features are quite frequent in early-type galaxies.

A.8. NGC4552 (M89, VCC1632)

NGC 4552 (M89) is characterised by diffuse filaments of ionised gas (Fig. 1). Some ionised gas in emission was detected by Macchetto et al. 1996. The morphology of the Hα filamentary structure is similar to the morphology observed in X-rays (Machacek et al. 2006a; Kraft et al. 2017; Kim et al. 2019). These filaments are not detected in absorption in the HST F555W (Fig. 6) or in the NGVS images. The hot-gas temperature varies radially, with a hot core, a decrease in temperature down to $T \sim$ 0.4 keV at 4-5 kpc, and an increase in the outer regions to $T \sim$ 0.6 keV (Kim et al. 2019). The asymmetric distribution of the hot gas indicates that the galaxy is ram pressure stripped while travelling within the cluster. The morphology of the hot gas of the galaxy at the interface with the surrounding ICM is due to the viscosity and the Kelvin-Helmholtz instabilities created in these gas layers (Roediger et al. 2015). NGC 4552 is a slow rotator (Emsellem et al. 2011) in which the gas kinematics is strongly decoupled from the stellar kinematics in the inner 320 pc (Sarzi et al. 2006), and it has a non-regular rotation (Krajnović et al. 2011). The deep optical NGVS image of the galaxy shown in Fig. 5 indicates shells and tidal tails, suggesting that this object underwent a strong gravitational perturbation (Penoyre et al. 2017; Pop et al. 2018). Although the galaxy cleary experienced a ram pressure stripping event during its journey within the cluster (Machacek et al. 2006a), the ionised gas filaments probably have an external origin and are gas that was accreted during the merging event and ionised by the shocks produced by the nuclear outflow (Machacek et al. 2006b).